Geomorphology 121 (2010) 30–54

Contents lists available at ScienceDirect

Geomorphology

journal homepage: www.elsevier.com/locate/geomorph

The sedimentology and dynamics of crater-affiliated wind streaks in western Arabia Terra, Mars and Patagonia, Argentina

J. Alexis. P. Rodriguez [a,*], Kenneth L. Tanaka [b], Aya Yamamoto [c], Daniel C. Berman [a], James R. Zimbelman [d], Jeffrey S. Kargel [e], Sho Sasaki [f], Yan Jinguo [g], Hideaki Miyamoto [h]

[a] Planetary Science Institute, 1700 E. Ft. Lowell Rd., Suite 106, Tucson, AZ, 85719, USA
[b] Astrogeology Science Center, U.S. Geological Survey, Flagstaff, Arizona, AZ 86001, USA
[c] RESTEC, Minatoku, Tokyo 106, Japan
[d] Center for Earth and Planetary Studies, National Air and Space Museum, Smithsonian Institution Washington, 20560, USA
[e] Hydrology & Water Resources, University of Arizona, Tucson, Arizona 85721, USA
[f] National Astronomical Observatory of Japan, 2-12 Hoshigaoka, Mizusawa, Oshu 023-0861, Japan
[g] State Key Laboratory of Information Engineering in Surveying, Mapping and Remote Sensing, Wuhan University, Wuhan, China, 430070
[h] University Museum, University of Tokyo, Tokyo 113-0033, Japan

ARTICLE INFO

Article history:
Received 5 August 2008
Received in revised form 6 July 2009
Accepted 29 July 2009
Available online 31 August 2009

Keywords:
Mars
Windstreaks
Aeolian
Resurfacing
Sediment transport

ABSTRACT

Wind streaks comprise recent aeolian deposits that have been extensively documented on Venus, Earth and Mars. Martian wind streaks are among the most abundant surface features on the planet and commonly extend from the downwind margins of impact craters. Previous studies of wind streaks emerging from crater interior deposits suggested that the mode of emplacement was primarily related to the deposition of silt-sized particles as these settled from plumes. We have performed geologic investigations of two wind streaks clusters; one situated in western Arabia Terra, a region in the northern hemisphere of Mars, and another in an analogous terrestrial site located in southern Patagonia, Argentina, where occurrences of wind streaks emanate from playas within maar craters. In both these regions we have identified bedforms in sedimentary deposits on crater floors, along wind-facing interior crater margins, and along wind streaks. These observations indicate that these deposits contain sand-sized particles and that sediment migration has occurred via saltation from crater interior deposits to wind streaks. In Arabia Terra and in Patagonia wind streaks initiate from crater floors that contain lithic and evaporitic sedimentary deposits, suggesting that the composition of wind streak source materials has played an important role in development. Spatial and topographic analyses suggest that regional clustering of wind streaks in the studied regions directly correlates to the areal density of craters with interior deposits, the degree of proximity of these deposits, and the craters' rim-to-floor depths. In addition, some (but not all) wind streaks within the studied clusters have propagated at comparable yearly (Earth years) rates. Extensive saltation is inferred to have been involved in its propagation based on the studied terrestrial wind streak that shows ripples and dunes on its surface and the Martian counterpart changes orientation toward the downslope direction where it extends into an impact crater.

1. Introduction

Much of the Martian surface is mantled with aeolian deposits. The study of these deposits is important to understand the interaction of the surface and the atmosphere (Greeley and Thompson, 2003). The deposits can also provide information on the reworking of sedimentary materials produced by a collection of surface geological processes, including fluvial, lacustrine, glacial, and volcanic activity as well as in situ mechanical and chemical weathering—all of which have been noted to occur on the surface of Mars (Baker, 1982; Carr, 1996; Kargel, 2004). Wind streaks are one type of aeolian deposit that occur on Mars (Figs. 1–3) and Earth (Fig. 4), but they are significantly more abundant on Mars, where they comprise widespread young aeolian features that typically occur in the lee of impact craters (Thomas et al., 1981; Lee, 1984) and have high length–width ratios (Greeley et al., 1974a,b; Maxwell and El-Baz, 1982; Greeley, 1986; Greeley et al., 1989; Zimbelman and Williams, 1996). Based on the inferred morphogenesis of Martian wind streaks, Thomas et al. (1981) classified them into three subsets, those produced: (1) by wind erosion and removal of surficial sediments from the lee of topographic obstacles; (2) from the preservation of surficial sediments located in the lee of topographic

* Corresponding author.
E-mail address: alexis@psi.edu (J.A.P. Rodriguez).

0169-555X/$ – see front matter © 2009 Elsevier B.V. All rights reserved.
doi:10.1016/j.geomorph.2009.07.020

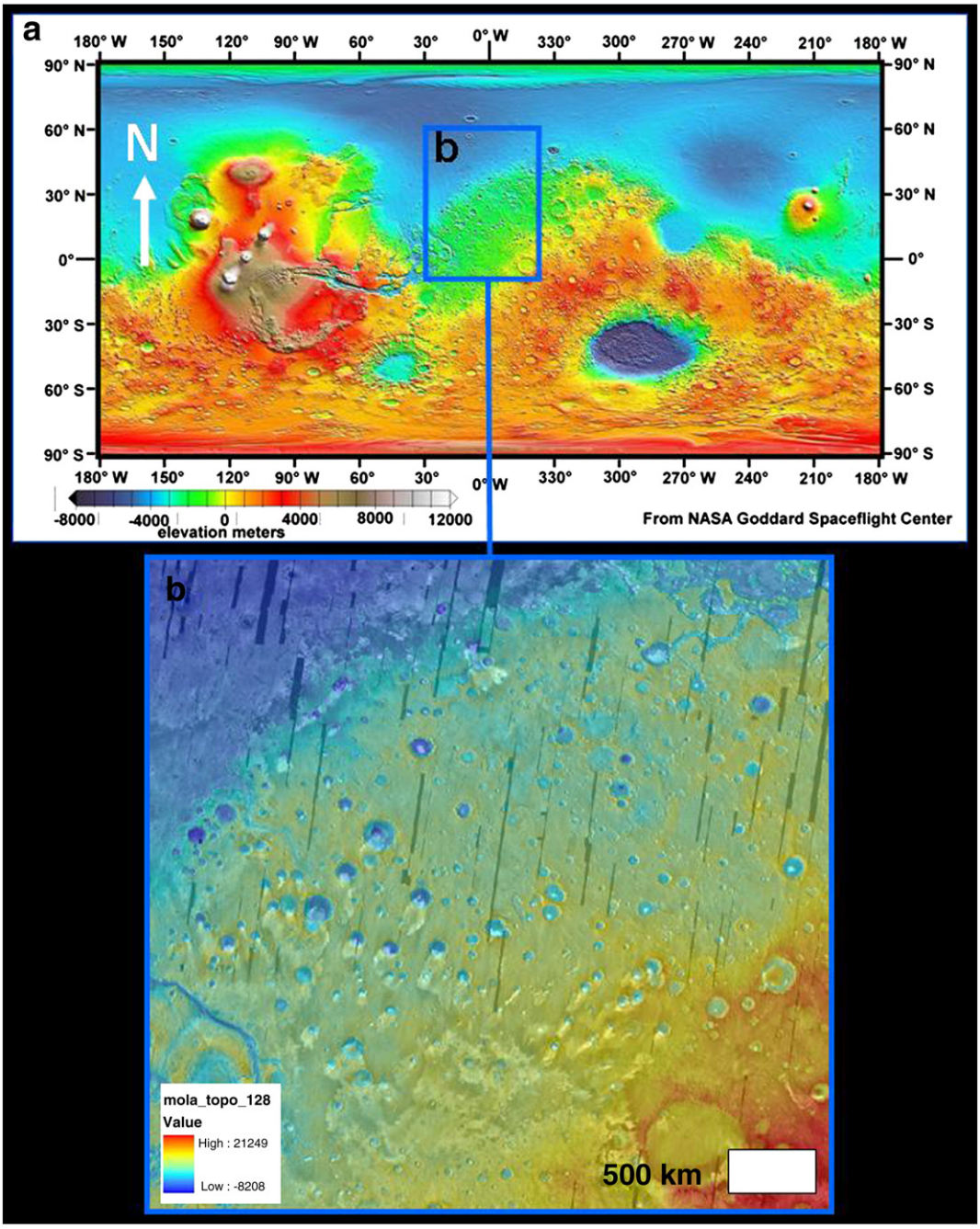

Fig. 1. (a) Color-elevation relief map of Mars (data from Mars Orbiter Laser Altimeter (MOLA), MGS mission, courtesy of NASA Goddard Spaceflight Center). Shown is the location of panel b, where western Arabia Terra is located. (b) Topography of western Arabia Terra. MOLA color-elevation relief map centered at 2°22′ E. 18°53′ N. (128 pixels per degree).

obstacles; and (3) by the aeolian deflation of sediments, typically intra-crater dune fields, and subsequent deposition downwind of the source.

Terrestrial wind streaks have been studied at several locations (Maxwell and El-Baz, 1982; Greeley and Iversen, 1985; Zimbelman, 1986; Greeley et al., 1989) and appear to have a variety of characteristics and origins (Zimbelman, 1986; Greeley et al., 1989; Zimbelman and Williams, 1996). Wind-tunnel modeling and fieldwork studies of wind streaks (Greeley et al., 1974a,b; Maxwell and El-Baz, 1982; Greeley, 1986; Greeley et al., 1989; Zimbelman and Williams, 1996) indicate that the formation of wind streaks involves three modes of sediment transport—saltation, traction, and suspension—and a range of particle sizes from clay through granules (Edgett, 2002).

The objective of this investigation is to improve our understanding regarding the morphogenesis of a cluster of crater-affiliated wind streaks in western Arabia Terra through the analysis of the higher resolution datasets now available, as well as through comparative planetary geomorphology. To do this, we have examined the spatial distribution (Fig. 2) and morphologic details (Figs. 5–13), and compared these to the results from our analysis of the morphologic and spatial attributes of a cluster of terrestrial wind streaks, which compare particularly well with those of the Arabia Terra wind streaks (Figs. 14–21).

Extensive areas of western Arabia Terra are covered by low-albedo wind streaks, each of which originates at a low-albedo area (e.g., Figs. 5–7). Low-albedo wind streaks and crater interior deposits

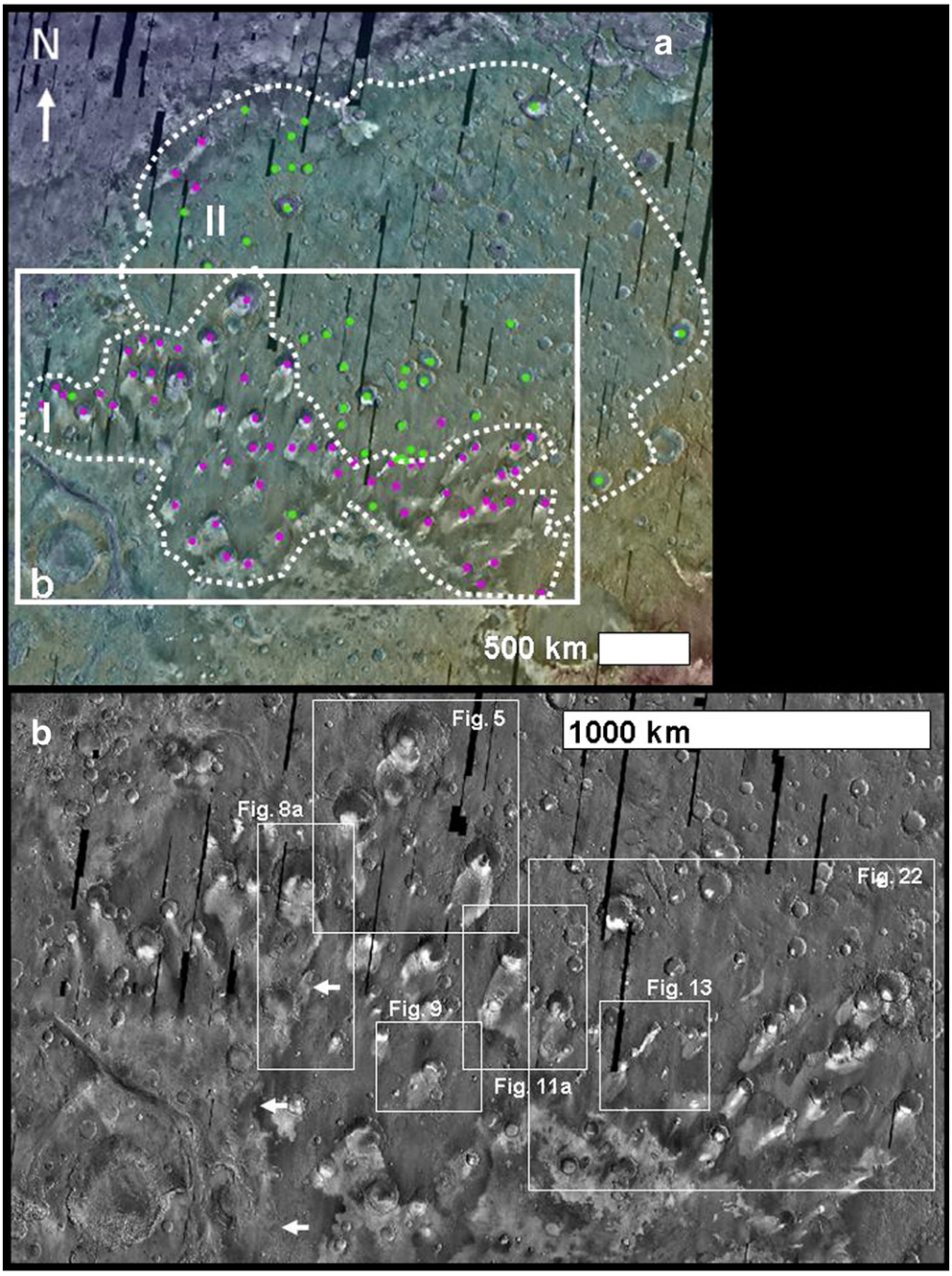

Fig. 2. (a) View of western Arabia Terra showing craters with low-albedo interior deposits that have well-developed wind streaks emanating from them (purple dots) and those that do not (green dots). Note that wind streaks form a cluster in zone I but are rare in zone II. Location of panel b outlined. (Part of THEMIS daytime IR mosaic (256 pixels per degree) supposed on MOLA DEM centered at 2°20′ E. 19°34′ N.) (b) Close-up view of panel a showing the locations for Figs. 5, 8a, 9, 11a, 13 and 22. (Part of THEMIS IR mosaic (256 pixels per degree)).

appear bright in Mars Odyssey's (ODY) Thermal Emission Imaging System infrared (THEMIS IR) daytime images (e.g., Figs. 2b, 8a, and 9a). Many of these wind streaks have high-albedo margins, resulting in a zoned appearance (white arrow in Fig. 5). Arabia Terra wind streaks extend many tens to a few hundred kilometers southeast or southwest and have been the subject of Mars geologic research since the early 1970s using image data from the Mariner 9 (Sagan et al., 1972, 1973; Arvidson, 1974), Viking Orbiter, (Soderblom et al., 1978; Thomas and Veverka, 1979; Kieffer et al., 1981; Peterfreund, 1981; Thomas et al., 1981; Thomas et al., 1984; Thomas and Veverka, 1986; Henry and Zimbelman, 1988; Presley and Arvidson, 1988; Arvidson et al., 1989; Strickland, 1989), and Mars Global Surveyor (Mustard, 1997; Cooper and Mustard, 1998; Edgett and Malin, 2000; Pelkey et al., 2001; Wyatt et al., 2001) missions. A few wind streaks similar to those in Arabia Terra occur in neighboring Xanthe Terra; in the opposite hemisphere to Arabia Terra near Marte Vallis, Tartarus Colles, and Gale crater (Thomas et al., 1981; Peterfreund, 1981; Zimbelman, 1986); and in at least one crater in the circum-polar plains of Planum Boreum (Fig. 3).

Wind streaks in western Arabia Terra have been interpreted to consist of primarily silt and/or fine sand-sized sediments transported via suspension from the low-albedo crater interior deposits where they originate (Edgett, 2002), and the thicknesses have been estimated to range from ~1 μm to 1 m (Pelkey et al., 2001; Edgett,

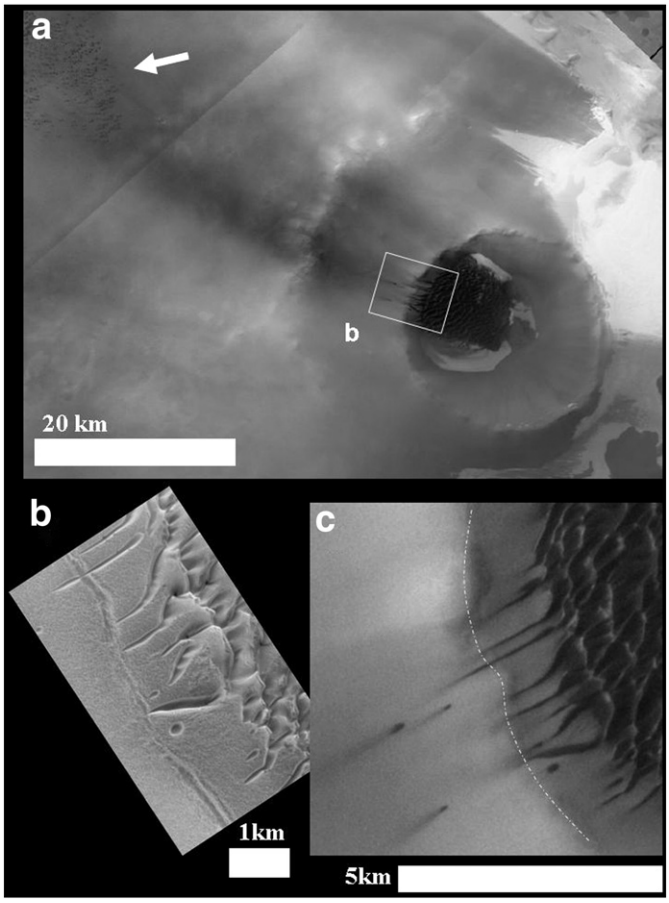

Fig. 3. (a) Impact crater along the margin of Planum Boreum (centered at 331.08° E. 78.61° N.). From THEMIS VIS north polar mosaic (courtesy of P. Christensen, Arizona State University). (b,c). Close-up views on the streaks extending across the crater rim (b, part of THEMIS VIS image V20583006 (20 m/pixel); and c, part of MOC image e1501692 (5.09 m/pixel)).

2002). Edgett (2002), however, found no evidence for plumes rising from western Arabia surfaces in any MOC images, nor were changes in the position, shape, or slip faces of intra-crater dunes identified from September 1997 to June 2001.

In most cases these low-albedo deposits consist of dune fields, interpreted to consist of primarily sand-sized particles (Edgett, 2002). In addition, most of these crater floors also exhibit eroded interior layered deposits, which are mostly light-toned (Edgett, 2002), many of which are interpreted to contain hydrated minerals (Poulet et al., 2008), deposited in ancient lakes (Poulet et al., 2008). Thermal emissivity data from Mars Global Surveyor's (MGS) Thermal Emission Spectrometer (TES) at 3 km by 6 km spatial resolution (Christensen et al., 1992; 2001) reveal that the intra-crater barchan dune fields in western Arabia Terra largely consist of TES Surface Type 1 (ST1) composition, interpreted as mostly unweathered basalts (Bandfield et al., 2000; Christensen et al., 2000; Hamilton et al., 2001; Wyatt and McSween, 2002; Wyatt et al., 2003), in contrast to the wind streaks that consist mostly of ST2, interpreted as basaltic andesite (Bandfield et al., 2000; Hamilton et al., 2001) or partly altered basalt (Minitti et al., 2002).

Thomas and Veverka (1979) observed that the wind streaks in western Arabia Terra change in terms of length and albedo relative to surrounding terrain on timescales short enough to have been observed between the Mariner 6 (1969), Mariner 9 (1972), and Viking orbiter (1976–1980) missions. Consistent with this observation, many streaks are different in MGS Mars Orbiter Camera Wide Angle (MOC WA) images from 1999 than they were when seen by the Viking orbiters (see Fig. 15 in Edgett, 2002). Relative to the surroundings, some streaks have not changed between MOC and Viking missions, others became lighter, some disappeared, and others grew longer (Edgett, 2002).

The terrestrial site that displays a cluster of wind streaks (Figs. 14–21) is in the Pali Aike Volcanic Field (52°S, 70°W), a region located in the southern Patagonian province of Santa Cruz in Argentina. Collectively, these streaks are known as the Pali Aike wind streak field (Fig. 4; (Rodriguez et al., 2008). Each wind streak in the comparable terrestrial region originates from sedimentary deposits within volcanic craters, which is similar to the impact crater sites of origin for the western Arabia Terra wind streaks. The Pali Aike Volcanic Field is located at northwest–southeast tectonovolcanic belt about 50 km wide and more than 150 km long, which consists of, two principal fracture systems of parallel or sub-parallel faults (Corbella, 2002; Zolitschka et al., 2006). The predominant fault system has an NW direction, followed by less frequent faults of E and ENE strike (Corbella and Chelotti, 1998). The NW system is emphasized by a regional alignment of geothermal anomalies (up to 6 °C/100 m) developed on the vertical of an underlying Jurassic rift zone that was formed during the breaking up of Gondwana (Corbella and Chelotti, 1998). The E and ENE fault system is parallel or sub-parallel to the faults and rift systems that seem to have channeled the large glacial valleys sub-perpendicular to the Andes such as the Magellan Strait, some fiords and bays and also the big Cordilleran lakes. All these valleys formed since 3.5 Ma and suggest a possible N–S stretch of the area because of a new strength field in the southern flank of the Magellan Basin (Corbella and Chelotti, 1998). These two normal fracture systems form a 60° conjugate fault system that allows, depending on the applied stress field, strike–slip transtensional and transcompressional openings accounting for the eruption of volcanics and the setting of scoria and ash cones and maars (Corbella and Chelotti, 1998). The Pali Aike Volcanic Field consists of alkali–olivine basalts with an age range of 3.8 Ma (Pliocene) in the western part to 0.01 Ma (Holocene) closer to the Atlantic Ocean (Corbella, 2002; Zolitschka et al., 2006). Cinder cones, lava domes, and about 100 maars (500–4000 m in diameter) were erupted mostly along fissures (Zolitschka et al., 2004, 2006).

The climate in the Pali Aike Volcanic Field ranges from arid to semi-arid and lacks any well-defined rainy seasons (Weischet, 1996). The meteorological record of the Rio Gallegos weather station ~60 km east of Pali Aike begins in 1931 (>75 years) but is rather fragmentary. It shows an annual mean precipitation of 251 ± 62 mm (missing values for 11 years) and a mean annual temperature of 7.4 ± 0.7 °C (missing values for 57 years), with a July (winter) minimum of + 1.0 ± 1.5 °C (missing 20 years) and a January (summer) maximum of 13.0 ± 1.2 °C (missing 17 years) (Zolitschka et al., 2006). Annual precipitation in Pali Aike is generally less than 300 mm (McCulloch et al., 2000; Gonzalez and Rial, 2004) and have been observed to be as low as 150 mm (Zolitschka et al., 2006). The mean annual temperature and annual precipitation in the Pali Aike volcanic field are 30–40% lower than the weather station in the coastal city of Rio Gallegos (Zolitschka et al., 2006). A characteristic of the Patagonian climate is the predominance of westerly winds, characterized by persistence during the year and also by intensity (Paruelo et al., 1998), with mean annual wind speed values of 7.4 m/s at Rio Gallegos. They are strongest in summer, and weakest in the winter (Baruth et al., 1998; Paruelo et al., 1998). Wind direction is primarily from the west, and shifts occasionally to NW and SW (Weischet, 1996; Baruth et al., 1998). During the winter, snow precipitation in the Pali Aike wind streak field occasionally buries the sedimentary deposits forming the surfaces of wind streaks and playas (e.g., Fig. 4b) and persistent subfreezing temperatures (Zolitschka et al., 2004) likely fix water-saturated sediments in playas. Comparisons of satellite images taken at different seasons, however, reveal that many of these lakes desiccate toward the end of the austral summer and are deflated by the prevailing westerly wind to deposit wind streaks (Zolitschka et al., 2006).

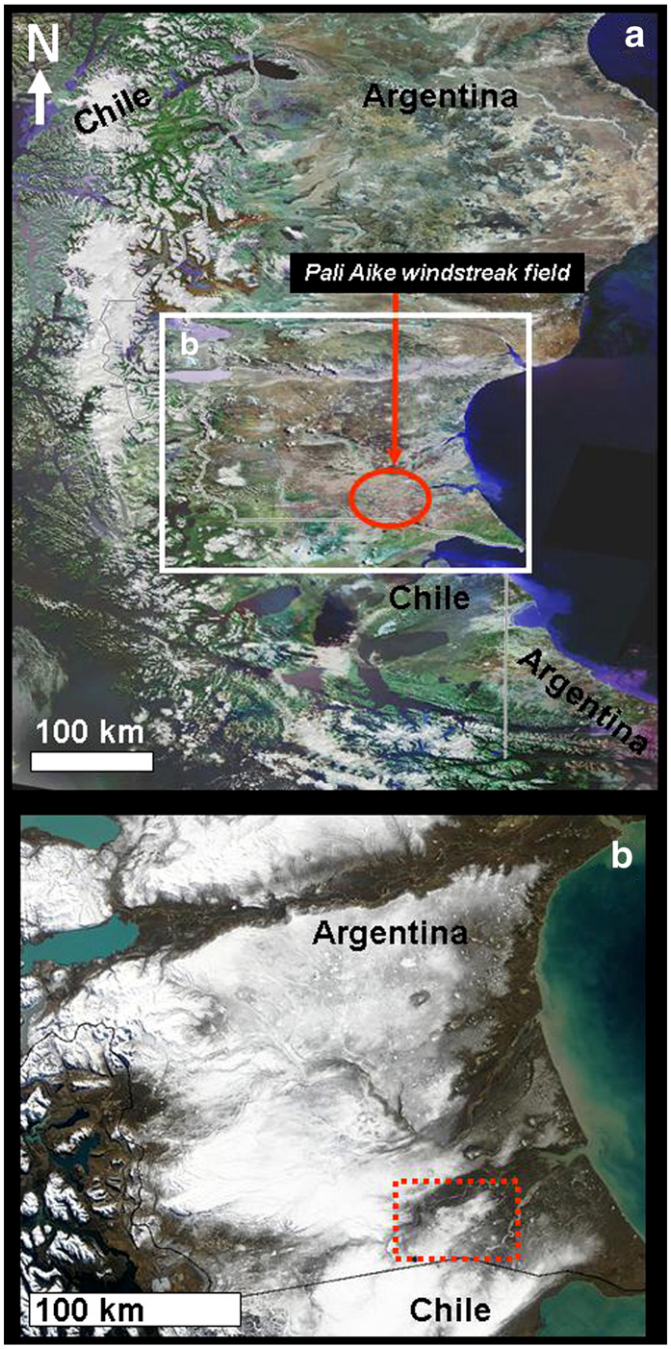

Fig. 4. (a) Context and location of the Pali Aike wind streak field in the Patagonian region of southern Argentina. Source Earth Satellite Corporation (http://www.earthsat.com/) (150 m/pixel). (b) Winter view of southern Patagonia. The Pali Aike wind streak field is delineated by red dots. True-color image from the Moderate Resolution Imaging Spectroradiometer (MODIS) on the Terra satellite, acquired August 14, 2002—http://veimages.gsfc.nasa.gov/4219/Patagonia.A2002226.1445.500 m.jpg).

Previous studies regarding the nature of the wind streaks in western Arabia Terra show that these wind streaks form by deflation of crater interior deposits, which generally include dune fields and high-albedo layered outcrops (Mustard, 1997; Cooper and Mustard, 1998; Edgett and Malin, 2000; Pelkey et al., 2001; Wyatt et al., 2001). Observations prior to HiRISE data indicate that wind streaks in this region were primarily emplace via suspension from air-borne dust/silt plumes (Edgett, 2002). Previous workers have recognized that at present in the Pali Aike Volcanic Field many maars and other volcanic craters contain ephemeral evaporative playas, whereas others hold saline lakes, and that some of the playas have associated wind streaks (Zolitschka et al., 2006). The new findings presented in this investigation that apply in western Arabia Terra and in Pali Aike include: (1) the transfer of sediments from crater interior deposits to and along the associated wind streaks has involved suspension of fines and saltation and traction of sand-sized sedimentary particles; (2) the composition, and not just grain size (e.g., Edgett, 2002), of the crater interior deposits is a key factor on whether or not wind streaks form; and (3) the formation of wind streak clusters may have resulted from the existence of relatively large, deep, closely-spaced craters containing interior deposits.

2. Datasets and methodology

Spatial measurements as well as morphologic and morphometric analyses were performed using GIS (Geographical Information Systems). To investigate the spatial and topographic attributes of wind streaks and craters with interior deposits in western Arabia Terra we have utilized spatially co-registered visible and infrared image data respectively obtained by the Viking orbiters and the Mars Odyssey (ODY) Thermal Emission Imaging System (THEMIS), as well as Mars Global Surveyor (MGS) Mars Orbiter Laser Altimeter (MOLA)-based digital elevation models. The study of sedimentary deposits modified by aeolian activity has been performed using image data from Mars Reconnaissance Orbiter (MRO) High Resolution Imaging Science Experiment (HiRISE) and Context (CTX) cameras, as well as the Mars Global Surveyor (MGS) Mars Orbiter Camera (MOC).

Our geomorphologic descriptions of the wind streaks in Pali Aike are based on the analysis of (1) Landsat 7 multi-band image data, (2) Advanced Spaceborne Thermal Emission and Reflection Radiometer (ASTER) spectral image data, (3) field reconnaissance observations obtained during January of 2005, and (4) a digital elevation model of the Pali Aike region using Shuttle Radar Topographic Mission (SRTM, spatial resolution is 90 m and vertical accuracy ± 10 m) data.

ASTER data (3-band visual and near-infrared (VNIR) data and 6-band short-wavelength infrared (SWIR) data) were atmospherically and geometrically corrected. Atmospheric corrections were performed using the ATCOR2 method (http://www.atcor.de), which is based on the modtran-program. VNIR data were used to obtain color and vegetation information and SWIR to obtain spectral information of carbonate and clay minerals. We used clustering classification, a method that uses all band data content. The target site data (corners at 51.74° S, 70.04° W; and 51.93° S, 69.61°) were subtracted from a whole scene of ASTER data (Fig. 15a). For geometric correction, we selected 20 tie points between an ASTER image and a high-resolution (2.4 m/pixel) QuickBird satellite image, and used a 1st-order polynomial equation to solve the relationship between the two images for geographic latitude and longitude according to the WGS84 datum. Following these corrections, we obtained atmospheric-effect-free images and georeferenced them in Google Earth. Next, a classification analysis on the 9-band target site image was performed. We chose the Iterative Self-Organizing Data Analysis Technique ISODATA clustering method (Swain, 1973; Tou and Rafael, 1974) as an objective classification approach. The ISODATA clustering method uses the minimum spectral distance to assign a cluster (class) for each candidate pixel. In this study, we set the number of classes to 20, the maximum iterations to 1000, and the convergence threshold to 0.95 for the classification rule. Fig. 15b was produced using the ASTER clustering classification. The vegetation and water classes were defined from their spectral information. The volcanic sediments (class 15) and carbonates (class 20), which were set as end members, were defined from the ground-truth information. The various degrees

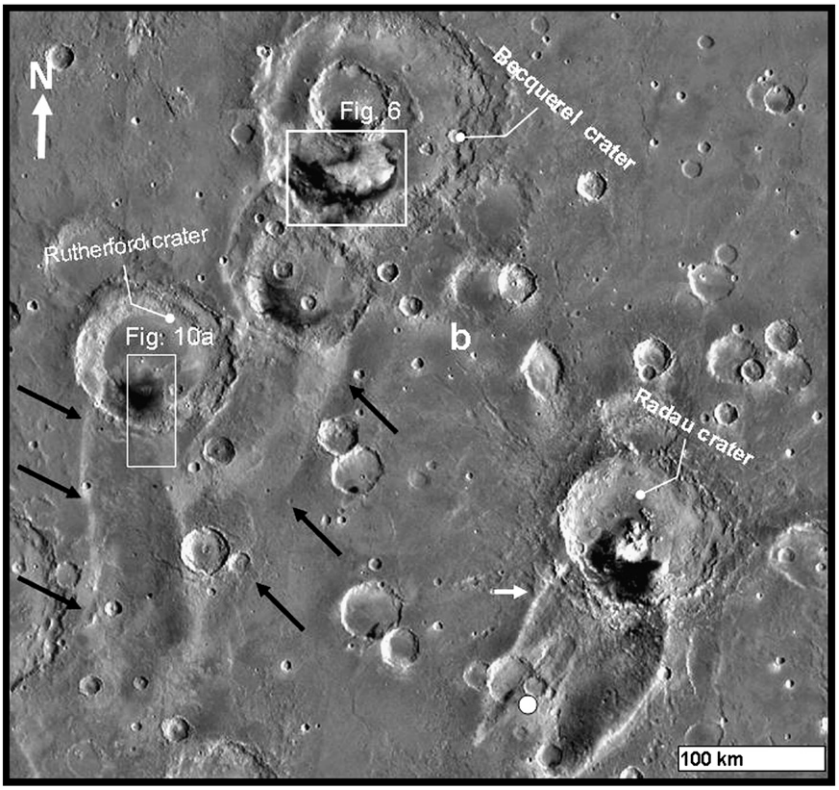

Fig. 5. (a) Crater chain including Becquerel crater in western Arabia Terra. See Fig. 2b for location and context. The locations of Figs. 6 and 10a are indicated. Notice a wind streak surrounded by a bright halo (white arrow) that emerges from Radau crater and extends into other craters, one of which contains low-albedo deposits that form the emergence zone of another wind streak (black arrow) (THEMIS daytime IR, 256 pixels/degree centered at 7°10′ W. 18°54′ N.).

of weathering and mixing were inferred by the other intermediate spectral classes.

The nearest-neighbor distance (NND) method involved measuring the closest distance between the center of high-albedo crater interior deposits, both for those that have and do not have associated wind streaks. Measurements of crater depths (maximum rim-to-floor vertical distance) and diameters were performed using Martian MOLA and Terrestrial SRTM DEMs. For consistency we have used

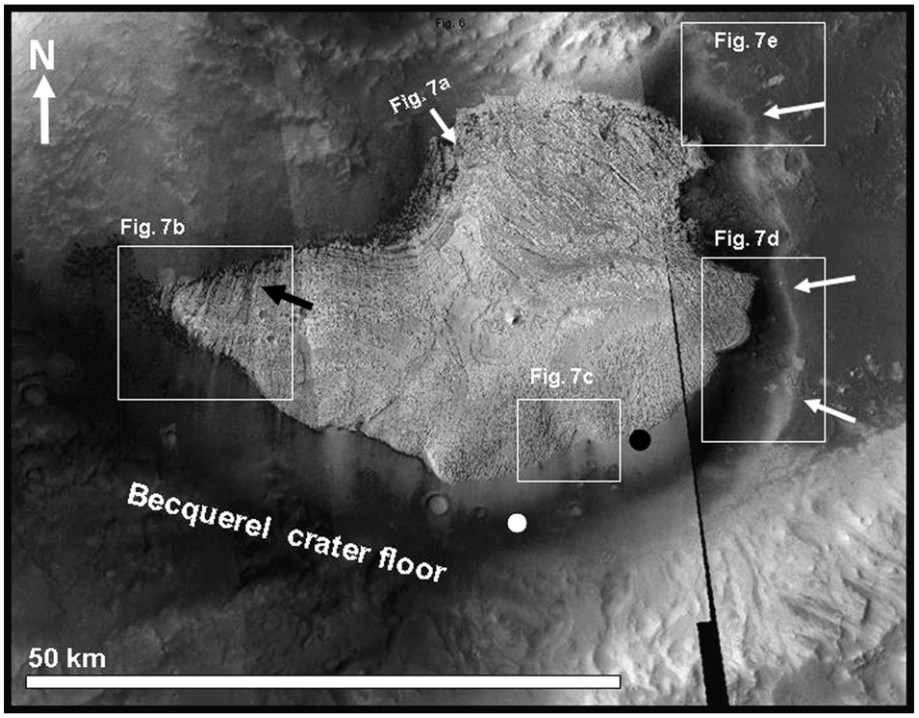

Fig. 6. CTX view (6 m/pixel) of the southern part of Becquerel crater centered at 8°3′ W. 21°16′ N. See Fig. 5 for context and location. Shown are dark streaks that extend across the light-toned layered deposits (black arrow), as well as dark (white dot) and bright (black dot) surfaces. The white arrows show the location of a bright halo.

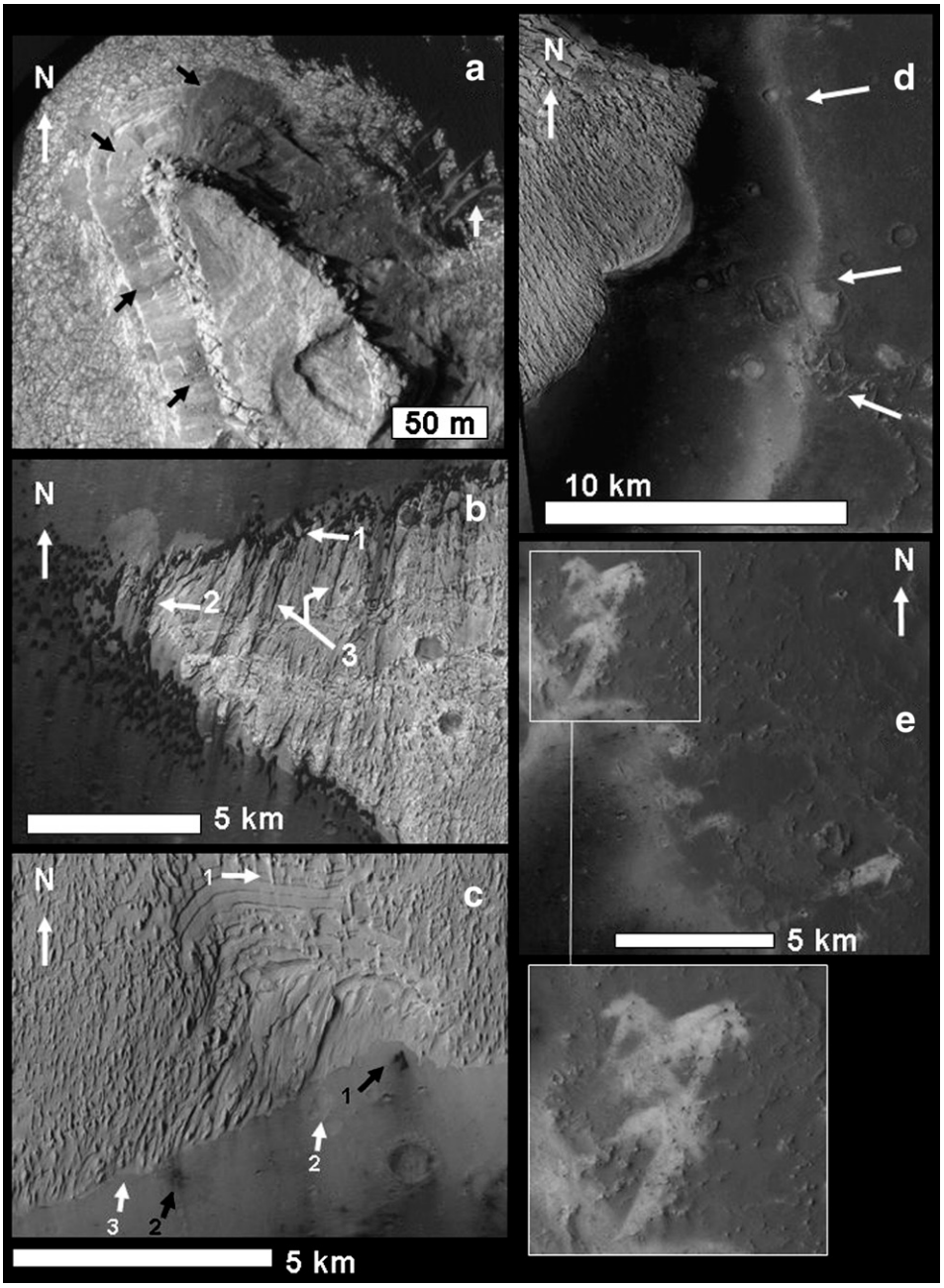

Fig. 7. Close-up views of the floor of Becquerel impact crater. See Fig. 6 for context and location. (a) Close-up view on irregular scarps adjacent to bouldery debris aprons. Our survey shows these are rare throughout the image. (Parts of HiRISE image PSP_001546_2015; 25 cm/pixel). (b,c,d, and e) Parts of CTX mosaic (6 m/pixel). Close-up views of the light-toned layered outcrop and surrounding bright and dark surfaces.

the largest diameter values where the craters were asymmetrical. To assess whether or not the means for the NND, the crater diameter values, and the crater rim-to-floor depth values are similar in the regions with and without wind streaks, we have used MATLAB to perform 2-tailed *t*-tests of six 2-sample groups using Matlab (see Appendix A for raw data). *T*-test (O'Mahony, 1986) assesses whether the means of two groups are statistically different from each other. The null hypothesis assumes that H_0: $\mu_1 = \mu_2$, where μ_1 = the mean of population 1, and μ_2 = the mean of population. If the *p*-value (i.e. the likelihood to get the same results if the null hypothesis was true) associated with the *t*-test is <0.05, evidence shows that the mean is significantly different than the hypothesized value (i.e. we reject the null hypothesis). If the *p*-value associated with the *t*-test is >0.05, we conclude that the evidence suggests that the mean is not different from the hypothesized value (we do not reject the null hypothesis).

3. Geomorphologic analysis

3.1. New morphologic insights of wind streaks in western Arabia Terra

Western Arabia Terra wind streaks commonly extend tens to hundreds of kilometers across cratered highland terrains (e.g., Figs. 1b and 2b) from craters that contain light-toned deposits, interpreted to contain hydrated minerals (Poulet et al., 2008), as well as dark barchan dune fields thought to be of basaltic composition (Bandfield et al., 2000; Hamilton et al., 2001). Some wind streaks merge downwind of craters to form extensive regional sedimentary deposits. For example, the black arrows in Fig. 5 outline a zone where various wind streaks extend from a sequence of closely-spaced craters in western Arabia Terra and merge to form a composite sedimentary mantle. In another example, the white arrows in Fig. 2b mark the

margins of a similar low-albedo deposit that extends from a mosaic of wind streaks. We measured 66 wind streaks in the region and find that they have a broad range in length-to-width ratios (range = 0.73 to 5.98; mean = 1.85 ± 0.95, where ± 0.95 is the 1-σ standard deviation). The lengths range from 10 km to 230 km, with a mean of 65 ± 45 km (for raw data see Table 1 in Appendix A).

3.1.1. Impact crater clustering vs. wind streak frequency

Our examination of the highland terrain of western Arabia Terra, outlined in Fig. 2a, resulted in 106 impact craters that contain low-albedo interior deposits. We find that 63% of these craters are a source of wind streaks. The remaining craters do not have associated wind streaks. To quantify the association between the observed spatial frequency of wind streaks and the apparent clustering of impact craters with interior deposits, we divided the study area into two terrains where impact crater interior deposits either have or do not have associated well-developed wind streaks (Fig. 2a). The surface area of the terrain that has wind streaks is 1,380,000 km^2, whereas the streak-free terrain is 2,660,000 km^2. The numbers of impact craters with interior deposits in each of these two regions are 67 craters in the terrain with wind streaks and 39 craters where wind streaks are absent. These values indicate on average of 20,600 km^2 per crater (or 49 craters per 10^6 km^2) and 68,200 km^2 per crater (or 15 craters per 10^6 km^2) for the regions with and without wind streaks, respectively.

We also measured the nearest-neighbor distance (NND) among impact craters with interior deposits in these regions (for raw data see Table 2 in Appendix A). Within the wind streak cluster, the NND ranges from 29 to 293 km and has a mean of 92 ± 47 km. Within the region where wind streaks do not extend from low-albedo interior deposits, the NND ranges from 21 to 676 km and has a mean of 123 ± 112 km. These values are comparable to the wind streak lengths. A *t*-test conducted on these two samples shows a *p*-value of 0.04339097, suggesting that the means are different. Therefore, NND values amongst impact craters with interior deposits located within the region that has wind streaks tend to be lower than those in the region without wind streaks.

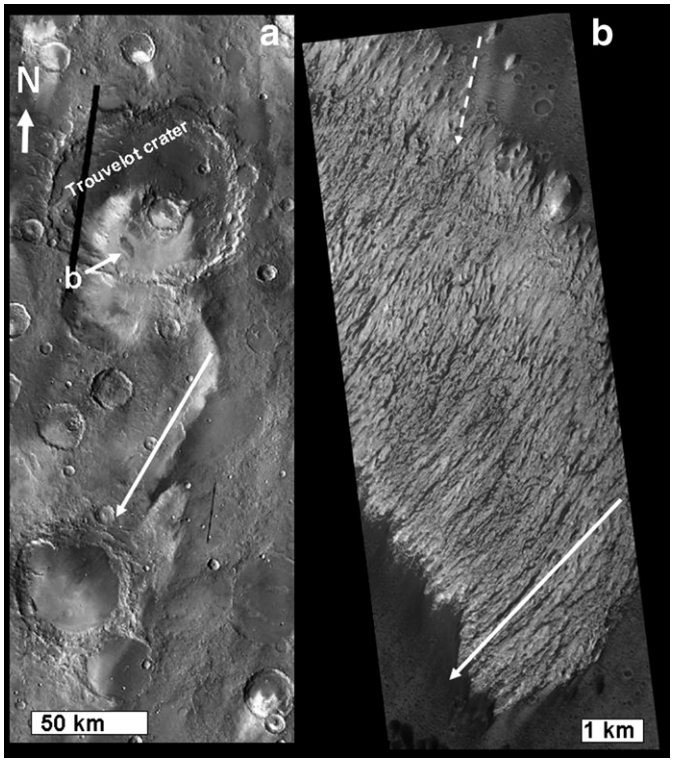

Fig. 8. (a) Trouvelot crater. Part of THEMIS daytime IR mosaic (centered at 13°6′ W., 16°12′ N.). See Fig. 2a for location and context. (b) Close-up view on the scoured surface of a high-albedo outcrop within the floor of the crater (Part of HiRISE image PSP_003287_1955; 25 cm/pixel).

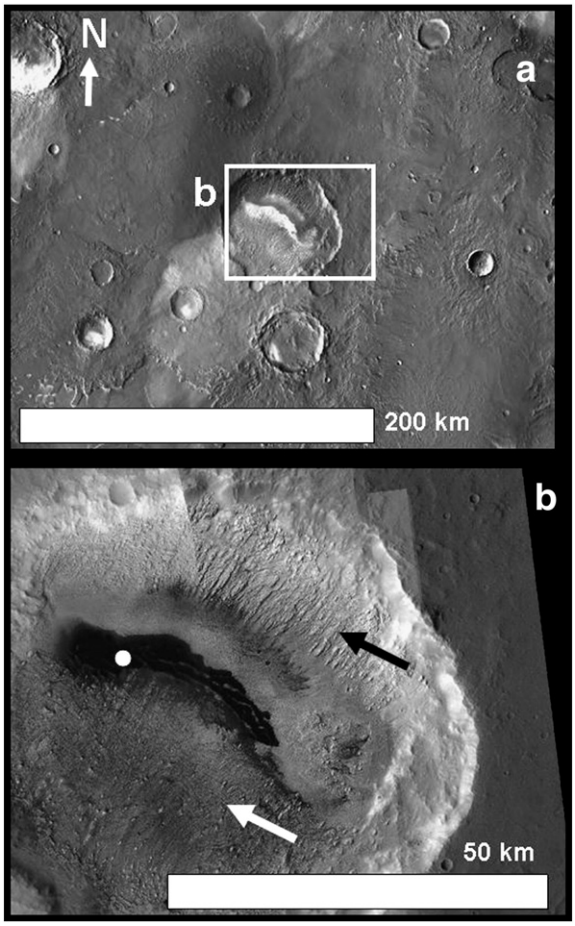

Fig. 9. Views of unnamed crater that displays extensive scour marks in its upwind and downwind margins (centered 7°1′ W., 8°6′ N.). See Fig. 2a for location and context. (a, part of THEMIS daytime IR mosaic; and b, part of CTX mosaic).

Finally, we have also estimated the depths and diameters of impact craters within both regions (for raw data see Table 3 in Appendix A). Within the wind streak cluster, impact crater diameters range from 25 to 175 km and have a mean of 64 ± 32 km. Crater depths range from 560 to 3000 m, with a mean of 1800 ± 600 m. On the other hand, within the region where wind streaks do not extend from low-albedo interior deposits, impact crater diameters range from 19 to 195 km and have a mean of 67 ± 33 km. Crater depths range from 200 to 3360 m, with a mean of 1400 ± 640 m. *T*-test conducted on these two pairs of samples shows *p*-values of 0.60819936 and 0.0014459472 for the diameter and depth datasets, respectively. These values suggest that whereas the crater diameters are similar in both regions, craters within the region with wind streaks tend to be deeper than in the region with no wind streaks.

In summary, we find that the location of the wind streak cluster in western Arabia Terra correlates to relatively higher areal density of impact craters with interior deposits, proximity of crater interior deposits, and crater depths. On the other hand, our measurements of crater dimensions in both the region with and the region without wind streaks, show similar values.

3.1.2. Impact crater interior deposits

Most impact craters in western Arabia Terra from which wind streaks emerge contain light-toned layered interior deposits as well as low-albedo barchan dune fields (Edgett, 2002) (e.g., Figs. 6–11). Fig. 6 shows a light-toned layered outcrop located in the southern floor of

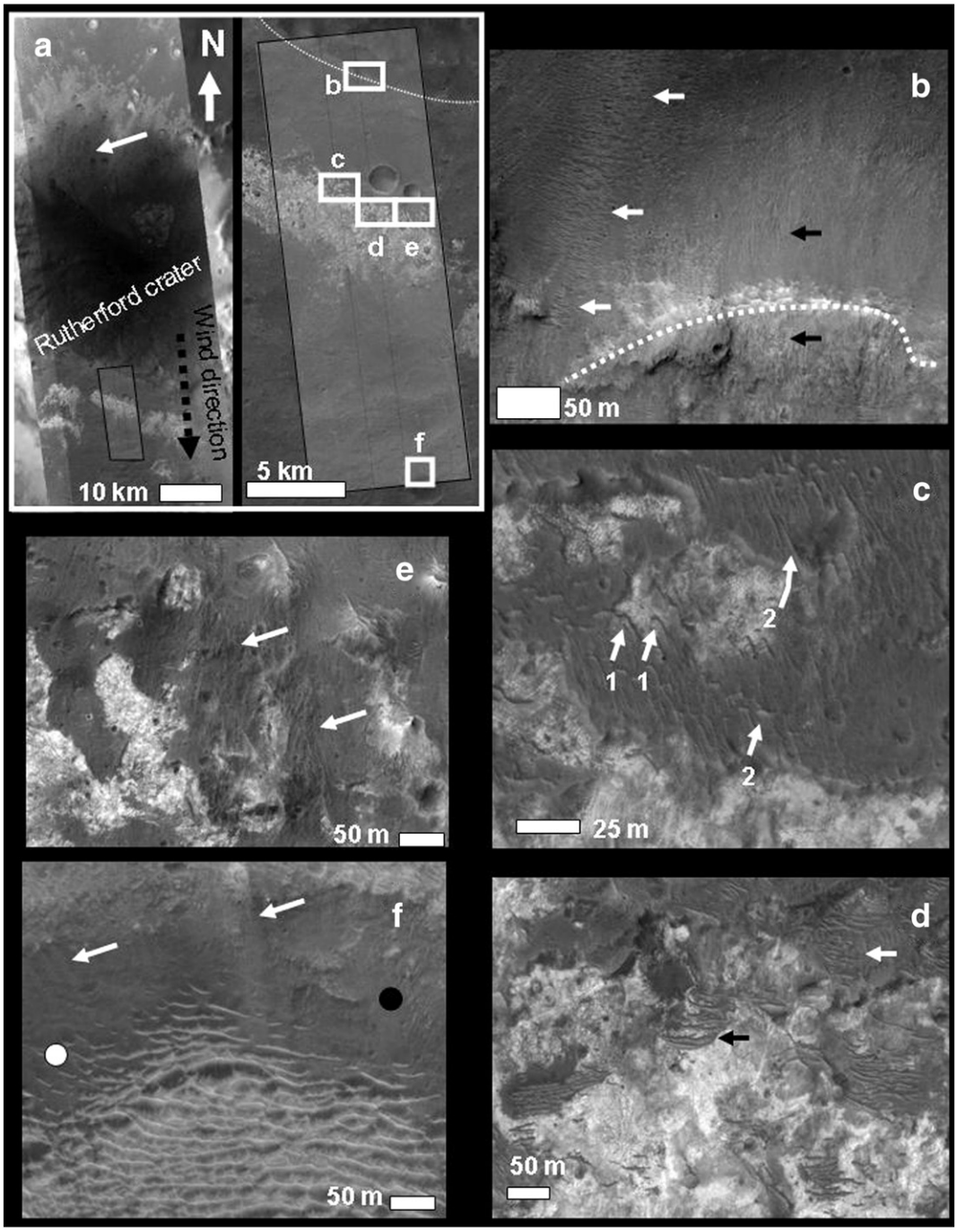

Fig. 10. (a) Left: View of Rutherford crater (centered at 10°41′ W., 19°11′ N.). See Fig. 5 for location and context. The location of HiRISE image PSP_008126_1985 is indicated (box). Right: The locations of panels b–f, which show close-up views on the wind streak surface, are indicated. The dashed line in a and b shows the location of the impact crater rim. See text for detailed descriptions.

Becquerel crater, which is surrounded by high- and low-albedo materials (black and white dots, respectively). Close-up views on this outcrop of high-albedo layered materials using HiRISE images reveal scarp fronts and adjacent bright boulder-rich debris aprons, perhaps produced by slope retreat (black arrows in Fig. 7a). Locally, these materials appear modified into bedforms (white arrow).

The black arrow in Fig. 6 shows dark streaks that locally extend across the surface of the outcrop. Higher-resolution images of this region show systems of low-albedo barchan dunes which in places climb (white arrow 1 in Fig. 7b) and extend across (white arrow 2 in Fig. 7b) the layered outcrop. Also the materials forming these dunes infill surface grooves in between yardangs (white arrows 3 in Fig. 7b).

Fig. 7c shows a zone where the layered high-albedo materials have been eroded into dense systems of yardangs. The white arrow 1 shows a yardang from which a high-albedo streak extends. In this region, the plains surrounding the layered outcrop consist of primarily high-albedo surface materials, which are locally rippled (white arrows 2 and 3).

The black arrow 1 in Fig. 7c shows a cluster of dome dunes from which a dark streak extends on top of the high-albedo surface. The black arrow 2 shows a dark ejecta blanket and surrounding ray system radial to an impact crater. Thus, it appears that low-albedo materials underlie and overlie the high-albedo materials in this region.

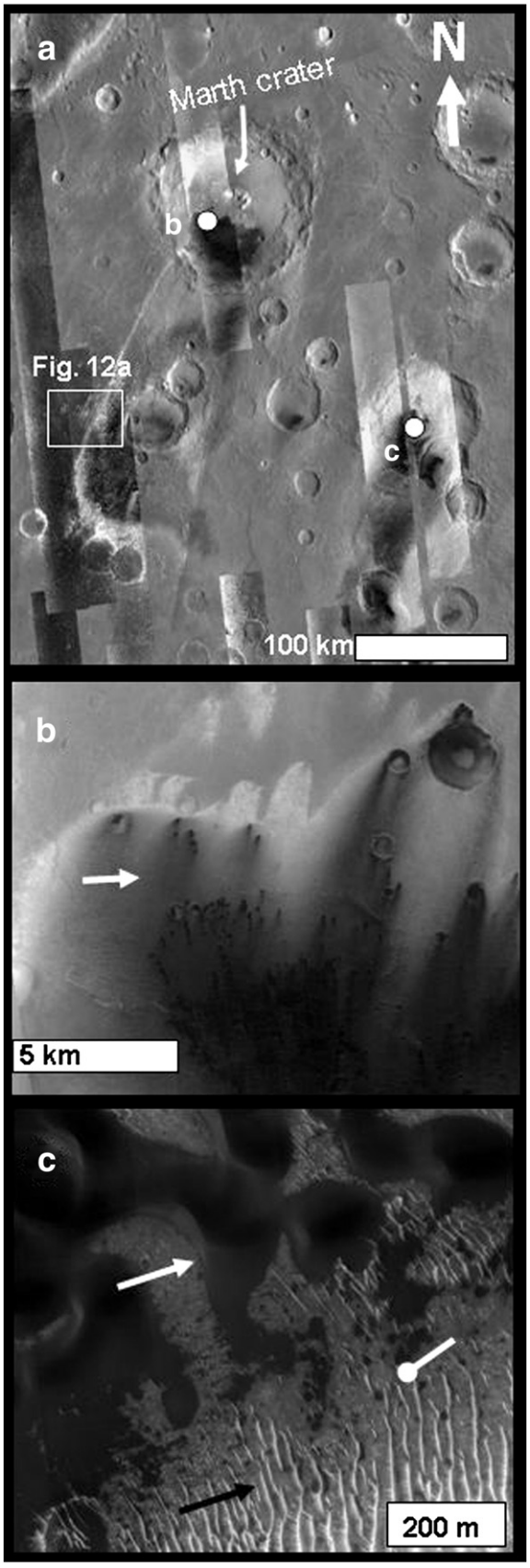

Fig. 11. (a) View of Marth crater (centered at 3°30′W, 12°59′N) and another unnamed crater (letter c). See Fig. 2b for context and location. (THEMIS daytime IR mosaic superposed by CTX images. The locations and contexts of panels b and c and Fig. 12a are shown. (b) Southern floor of Marth crater. (Part of CTX mosaic). (c) Interior deposits within a crater located approximately 200 km southeast of Marth crater. (Part of HiRISE image PSP_006504_1910).

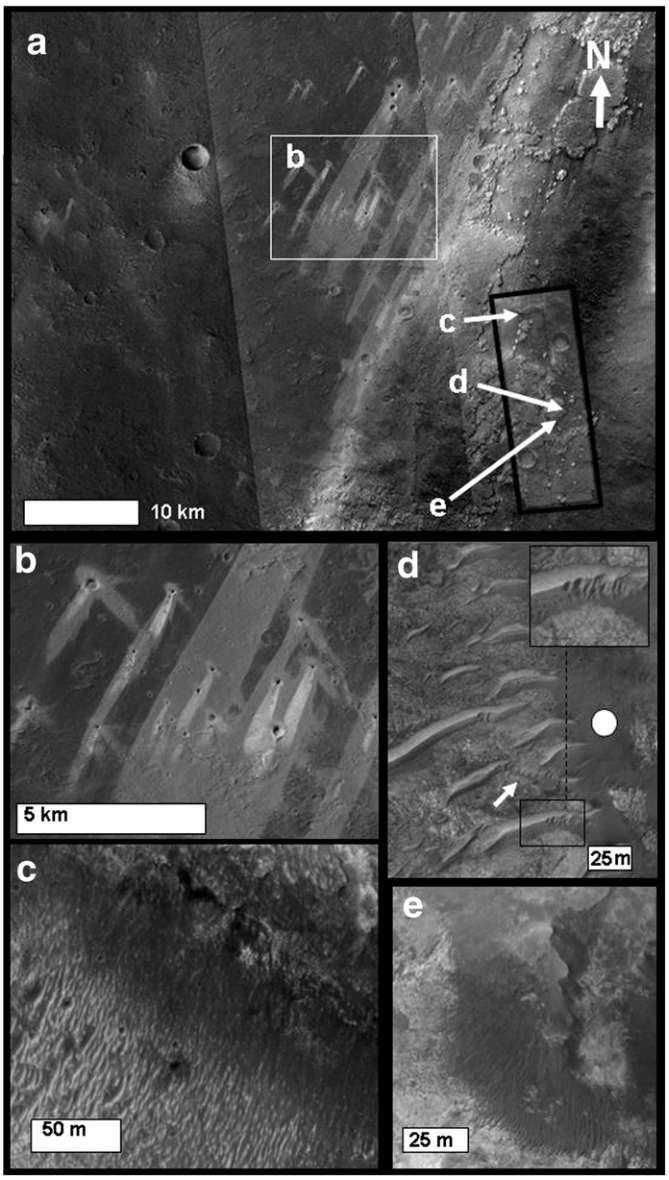

Fig. 12. (a) Close-up of a CTX mosaic covering part of the high-albedo margin of a wind streak. Context and location shown in Fig. 11a. Outlined is the location of HiRISE image PSP_009576_1905. (b) Close-up of part of panel a. (c,d, and e) Morphologic details of the wind streak surface. (Parts of HiRISE image PSP_009576_1905).

The eastern margin of the light-toned layered outcrop shows a high-albedo halo around low-albedo materials (white arrows in Figs. 6 and 7d). Similarly, wind streaks in western Arabia Terra also commonly display high-albedo margins (e.g., Figs. 5 and 12). Fig. 7d shows a zone adjacent to the high-albedo halo where systems of overlapping high-albedo streaks are preserved in various orientations.

Trouvelot crater also contains an outcrop of high-albedo materials. This outcrop displays surface grooves, interpreted to be yardangs. The orientation of the wind streak that emerges from the crater (white arrow in Fig. 8a) parallels the direction of the yardangs (white arrow in Fig. 8b). Fig. 9 shows the surface of an unnamed crater floor where features that we propose are yardangs are present on the upwind (black arrow in Fig. 9b) and downwind (white arrow in Fig. 9b) sides of the crater floor, which also contains low-albedo crater interior deposits (white dot in Fig. 9b). As in the case for Trouvelot crater, the orientation of the grooves is parallel to the axis of the wind streak.

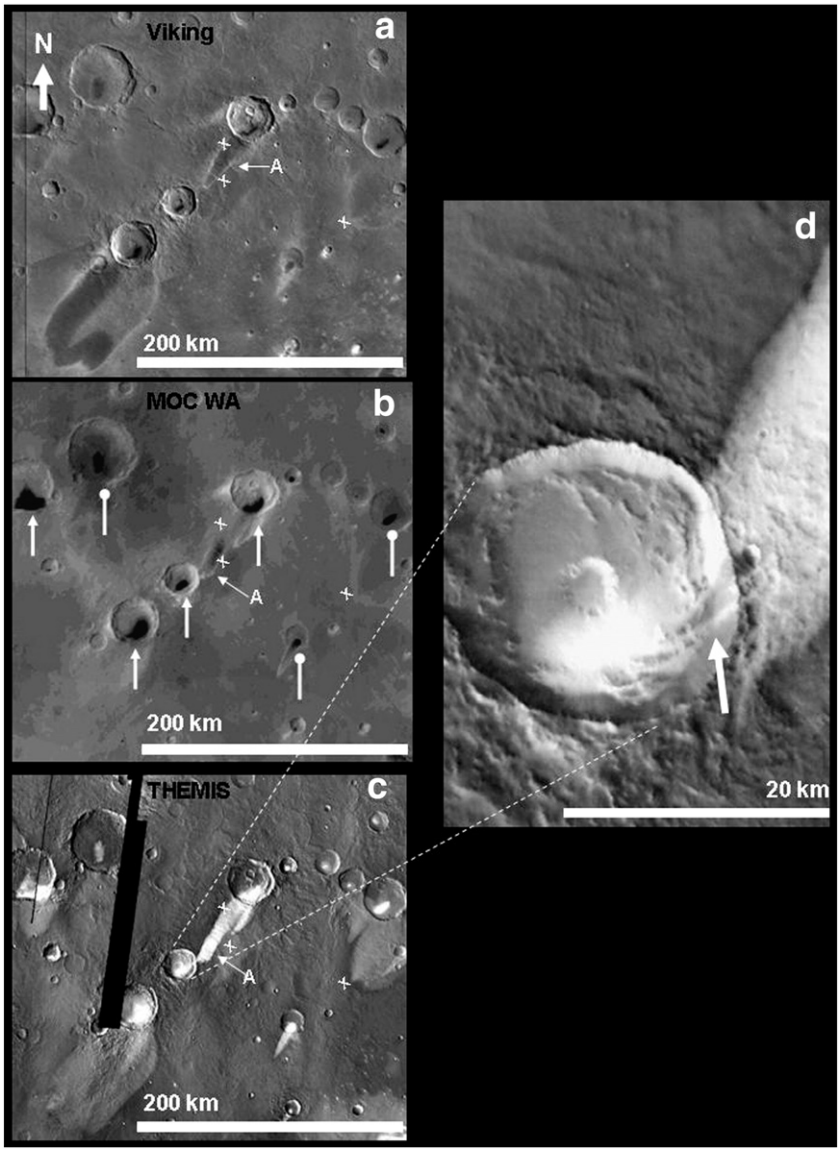

Fig. 13. Views of the same region in western Arabia Terra (centered at 9.1° N., 2.2° E.). Images in panels a,b and c were respectively extracted from global mosaics produced from Viking, MOC WA, and THEMIS daytime IR datasets. X's in all panels show the same locations. The Viking image in panel a was taken in 1978, whereas the MOC WA (wide-angle) mosaic was assembled from red images acquired in May–June 1999 from the Mars Orbiter Camera. The THEMIS mosaic was compiled using images obtained between the years 2002 and 2006. (d) THEMIS IR image I25598011 obtained in 2004 shows how the wind streak has propagated onto the impact crater's interior.

Mixing of low- and high-albedo streaks has produced zones of intermediate-albedo on the floors of Rutherford and Marth craters (white arrows in Figs. 10a and 11a and b, respectively). A close-up view of an unnamed crater 200 km SE of Marth crater (Fig. 11a) shows high-, intermediate- and low-albedo interior deposits (black arrow, white pointer and white arrow in Fig. 11c, respectively). The high-albedo materials are rippled, and embayed by the intermediate-albedo deposits, and the low-albedo materials form dunes, which overlie the other surface materials (Fig. 11c).

3.1.3. Bedforms in impact crater wind-facing slopes and along the wind streaks

Fig. 10b shows the wind-facing margin of Rutherford crater, where light-toned small dunes or large ripples (white arrows), as well as systems of ridges and scour marks (black arrows), extend to and across the crater rim. The wind streak that extends from Rutherford crater shows linear dune-like forms of intermediate-albedo oriented parallel to the orientation of the wind streak orientation on brighter basement materials (1 in Fig. 10c) and on overlying low-albedo materials (2 in Fig. 10c). We also observe transverse dunes, which are oriented perpendicular to the long axis of the wind streak, and which extend across mantles (white arrow in Fig. 10d) and exhumed light-toned materials (black arrow in Fig. 10d). Surface scour marks indicate locally modified low-albedo mantles (white arrows in Fig. 10e). The white dot in Fig. 10f shows low-albedo materials embaying high-albedo barchanoid dunes within a crater. The locations of light-toned streaks on top of the low-albedo materials are indicated by the white arrows, and the black dot shows a grooved surface.

On the other hand, along the wind streak that originates at Marth crater, we have observed systems of high-albedo dunes and ripples, which are embayed by low-albedo ripples (Figs. 11a and 12c–e). A close-up of the margin of the wind streak extending from Marth crater shows that the high-albedo halo surrounding it includes high-albedo rippled materials (Fig. 11c). In a terrain adjacent to this halo zone we have identified clusters of high-albedo streaks that extend in multiple directions radially from impact craters (Fig. 11a and b).

Although not in our study area, we have identified another dark wind streak which extends from a low-albedo barchan dune field within an impact crater along the margin of Planum Boreum (Fig. 3). Notice that the wind streak passes downwind into a dune field (white

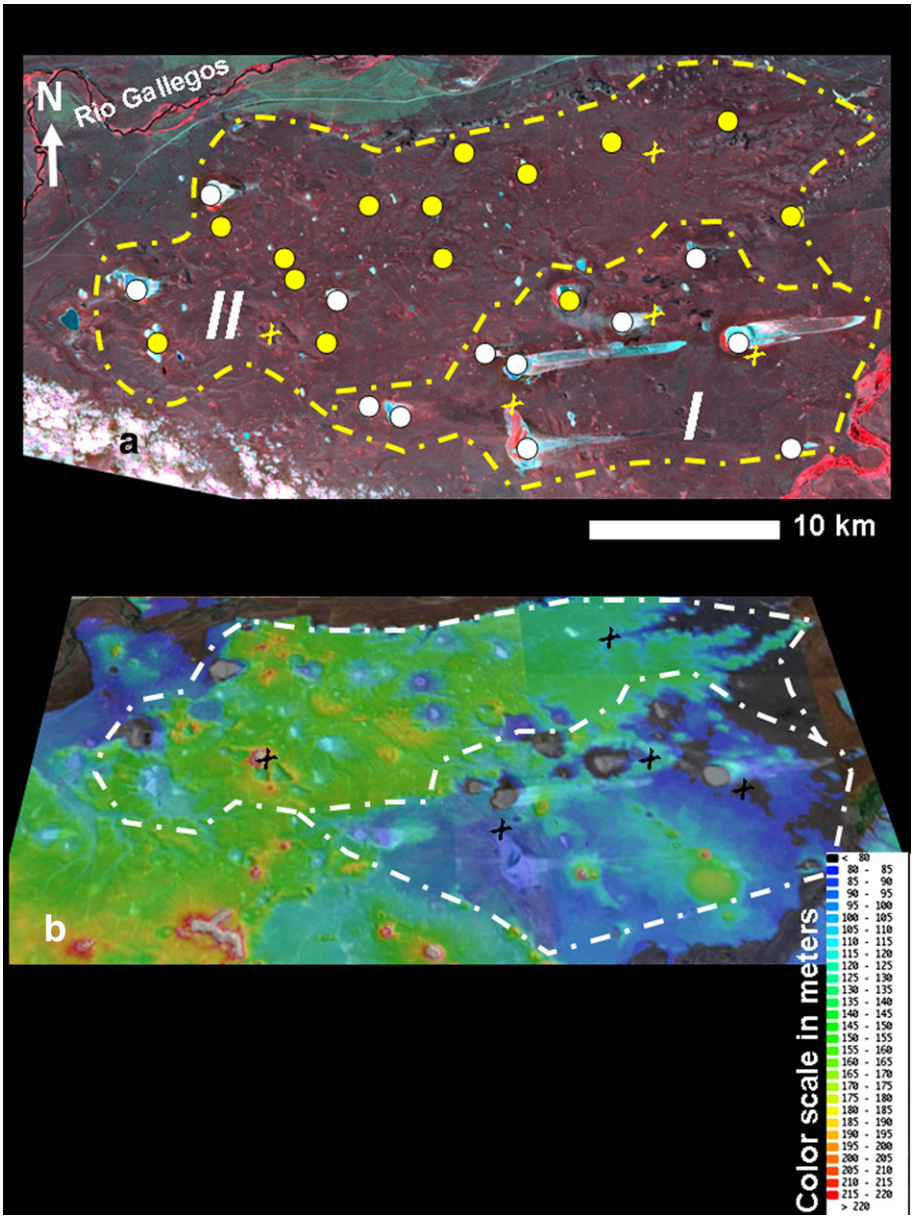

Fig. 14. (a) View of the Pali Aike region in Patagonia. Zones I and II (outlined by yellow lines) represent regions where most craters with playa interior deposits (>1 km across) display (white dots) or lack (yellow dots) associated wind streaks. (Atmospherically and geometrically corrected false-color ASTER image shows NIR, red, and green channels as the RGB components, respectively). (b) DTM (from Shuttle Radar data) superposed on Google Earth ASTER image base. The X marks in both panels show the same locations.

arrow in Fig. 3a). Horns extending from barchan dunes (white arrow in Fig. 3b) climb the inner wall of the crater and extend beyond the rim (dashed white line in Fig. 3b and c) and become diffuse into a low-albedo surface.

In summary, surface ripples, dunes, and scour marks have been observed to extend from wind-facing impact crater margins and onto the surface of associated wind streaks. The orientations of these features conform to the wind direction as inferred from the shapes of the wind streaks shapes. Thus, evidence suggests that sediments migrating by saltation out of impact crater interior deposits form a source of materials for the wind streaks in the downwind direction.

3.1.4. Recent changes in crater interior deposits and wind streak morphologies

A time series of images obtained in 1978 and 1999 show how a wind streak has propagated 10 km during the 21-Earth year interval into an impact crater in the downwind direction (letter A in Fig. 13). Where the wind streak extends into the impact crater, its orientation changes to conform to the downslope direction (Fig. 13d). The shapes of other wind streaks in the region have not changed significantly during this time interval (Fig. 13). Also during this time, some low-albedo crater interior deposits in the region appear to have increased in area significantly and others appear to have retained similar shapes and dimensions (white arrows and white pointers respectively in Fig. 13).

3.2. General morphologic attributes of Pali Aike wind streaks, Argentina

Our examination of a part of the regional plains of Pali Aike (Fig. 14) reveals a large number of volcanic craters, of which only 11 out of a total of 27 craters containing playa deposits show associated wind streaks. Our measurements of 11 wind streaks reveal a broad range in the length-to-width ratios (range = 0.05 to 8.02; mean = 3.0 ± 2.6), and the lengths (range = 0.7 to 9 km; mean = 3.1 ± 3.0 km) (for raw data see Table 4 in Appendix A). In this region, wind streaks occur as isolated features, and we have not observed zones

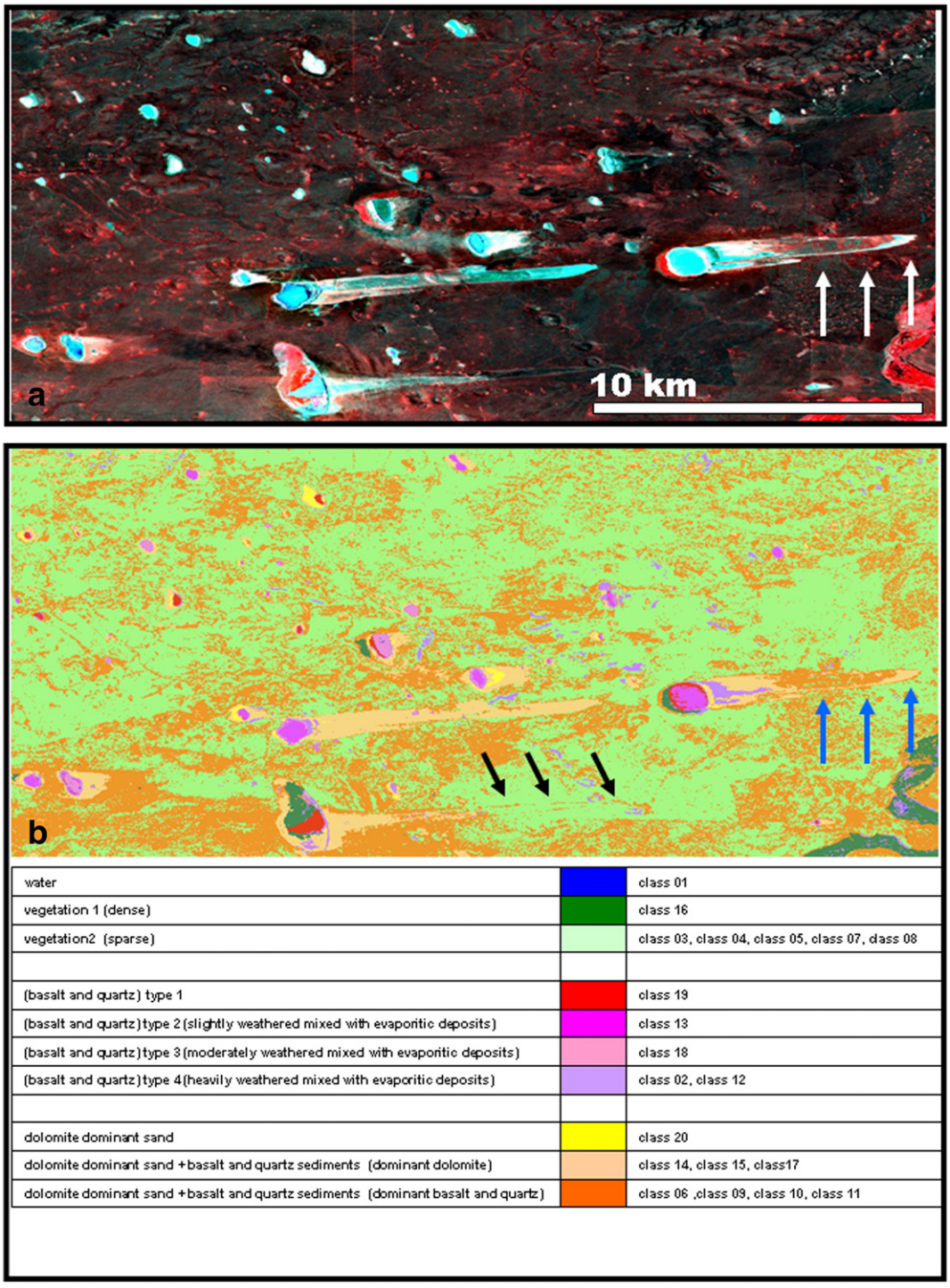

Fig. 15. (a) Target site image of ASTER data in false-color combination (RGB: band 3, band 2, and band 1). (b) Classification result of the target site.

where they overlap or extend into craters aligned in the downwind direction. The surfaces over which the Patagonian winds streaks propagate include terrains that vary 150 m in elevation (Fig. 15b). Promontories, such as the scoria cone shown in Figs. 17 and 20a (yellow arrows), do not appear to have affected the direction of wind streak propagation.

3.2.1. Crater clustering vs. wind streak frequency

We have identified two distinct zones in the region of study: Zone I in Fig. 14a outlines a cluster of 10 wind streaks, each of which initiates at an intra-crater playa deposit. The surface area of this zone is 100 km^2 (or 10 km^2 per crater). Zone II in Fig. 14a on the other hand outlines a terrain where 17 intra-crater playas occur, which mostly do not have associated wind streaks. The surface area of this zone is 180 km^2 (or 11 km^2 per crater).

We also measured the nearest-neighbor distance (NND) among playa craters in Pali Aike (for raw data see Table 5 in Appendix A). We find that: (1) within the wind streak cluster, the NND ranges from 1.31 to 6.58 km and has a mean of 3.33 ± 1.89 km, and (2) within the region where wind streaks do not extend from playa deposits, the

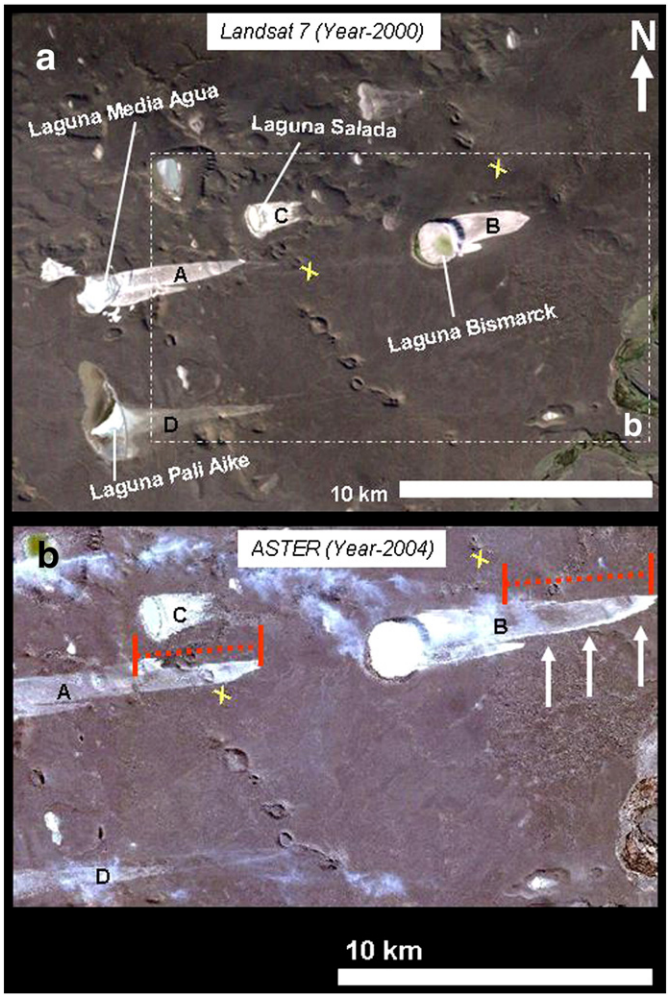

Fig. 16. (a) View of the Pali Aike wind streaks (letters A–D) from a simulated natural-color Landsat 7 dataset by TerraMetrics (ca. 2000). (b) ASTER image taken in September 2004, which shows a close-up view of the region. The yellow × letters show the same locations in panels a and b. The wisps at the top appear to be high-altitude cirrocumulus clouds.

NND ranges from 1.23 to 6.09 km and has a mean of 3.24 ± 1.52 km. A *t*-test conducted on these two samples shows a *p*-value of 0.8954064, suggesting that the means are similar.

Finally, we have also estimated the depths and diameters of impact craters within both regions (for raw data see Table 6 in Appendix A). Within the wind streak cluster, crater diameters range from 1439 to 3996 m and have a mean of 2171 ± 822 km. Crater depths range from 28 to 109 m, with a mean of 53 ± 24.6 m. On the other hand, within the region where wind streaks do not extend from crater interior playa deposits, crater diameters range from 925 to 3207 m and have a mean of 1985 ± 714 m. Crater depths range from 13 to 85 m, with a mean of 44.42 ± 20.76 m. *T*-test conducted on these two pairs of samples shows *p*-values of 0.56144804 and 0.33430636 for the diameter and depth datasets, respectively. These values suggest that whereas the crater diameters are similar in both regions, craters within the region with wind streaks tend to be deeper than in the region with no wind streaks.

In summary, we find that the location of the wind streak cluster in Pali Aike correlates to relatively higher areal density of impact craters with interior deposits and crater depths. On the other hand, our measurements of crater dimensions and proximity of crater interior deposits, in both the region with and the region without wind streaks, show similar values.

3.2.2. ASTER classification results

A classified ASTER image reveals that in Pali Aike, the crater interior deposits and the wind streaks that propagate from them include basalt, quartz and evaporitic (dolomite) sediments (Fig. 15). The features show various degrees of weathering and lithic abundances, yet no clear indication of a consistent change in composition along the downwind direction (Fig. 15). The provenance of the wind streak forming sediments may include regionally eroded sediments from (1) the Pliocene to late Quaternary Pali Aike volcanic landforms, (2) Oligocene marine sediments (sandstones and shales) related to a Tertiary marine transgression (Patagonia formation), (3) lower Miocene fine-grained molasse-type fluvial sediments (Santa Cruz Formation), (4) Pliocene and Pleistocene fluvioglacial deposits (Patagonian Gravel Formation), which form the surface of the southern Patagonian Plains today, (Zolitschka et al., 2006) and (5) dust derived from Patagonia during three glacial stages (stage 2, 18 ka (Last Glacial Maximum); stage 4, 60 ka; and stage 6, 160 ka) (Basile et al., 1997).

Some wind streaks in Pali Aike display high-albedo margins (e.g., Figs. 15b and 16b (white arrows)). The blue arrows in Fig. 15b indicate the location of a high-albedo margin of a wind streak that appears to consist of predominantly dolomitic sands.

We identified one wind streak that has a diffuse eastern end (letter D in Figs. 16 and 17). The black arrows in Fig. 15b show how

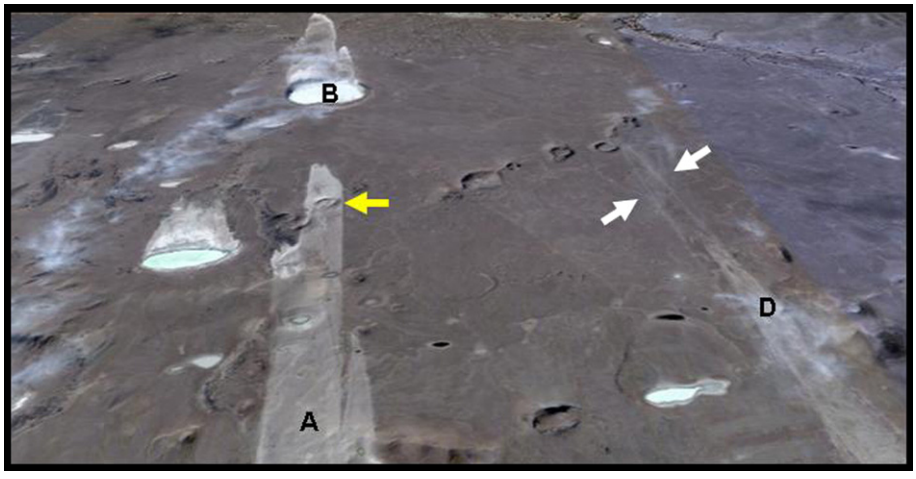

Fig. 17. Perspective view toward the east of zone where wind streaks A, B and D occur (image mosaics from Google Earth; courtesy of Google, Inc.).

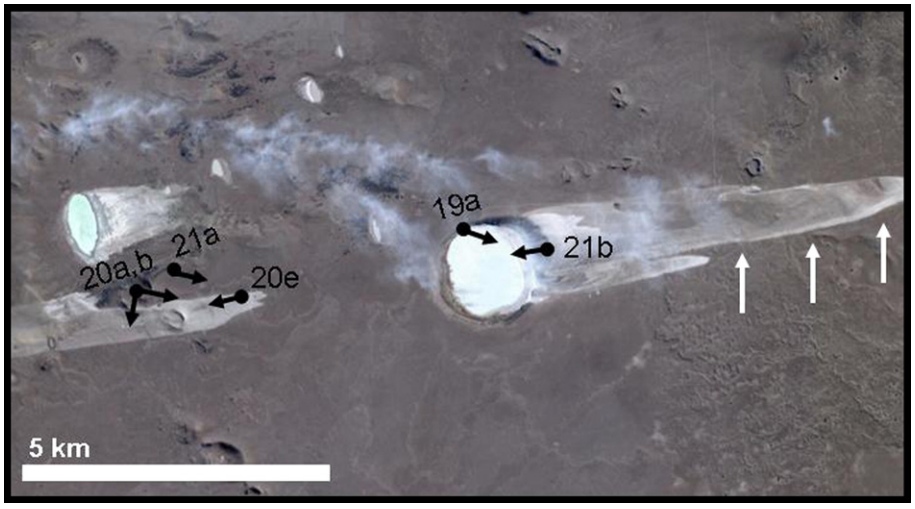

Fig. 18. Context view showing the locations and view points of images shown in Figs. 19a; 20a,b,e; and 21a,b (image mosaics from Google Earth; courtesy of Google, Inc.).

the diffuse zone in this wind streak is largely covered by vegetation, except around some margins where the outline of the wind streak is preserved in materials consisting of volcanic and dolomitic sands. These observations suggest that either these margins consist of thicker deposits or that they have undergone a lesser extent of dissipation due to perhaps relatively higher induration.

3.2.3. Evidence for recent wind streak propagation

A comparison between images taken during the years 2000 and 2004 reveals that some of the wind streaks in Pali Aike have extended downwind. For example letters A and B in Fig. 16 show wind streak that have, respectively, lengthened by 3.5 km (875 m/yr) and 4.9 km (1220 m/yr) during the four-year interval (red segments in panel b of Fig. 16b). Others show no significant change in shape or size (letters C and D in Fig. 16, letter D in Fig. 17).

3.2.4. Field reconnaissance observations

Observations made during a brief field reconnaissance (Fig. 18) during January, 2005 by author J.A.P. Rodriguez show that:

- The surface of the visited playa includes high- and low-albedo deposits (white and yellow arrows in Fig. 19, respectively). The latter form ramps along the downwind playa margin, where they also infill surface grooves (white arrows in panels b and c of Fig. 19). The playa surface is marked by ripples, which consist of darker coarser materials (crests), and lighter finer-grained materials (sides), but no dunes were identified (Fig. 19d).
- The visited wind streak displays sharp margins across its whole surveyed zone (Fig. 20), it extends over a scoria cone (yellow arrow in Fig. 20a), it is locally rippled (Fig. 20e), and at least one dune has formed along its path (white pointer in Fig. 20a).
- Embayment relationships of grassland suggest that the wind streak has a thickness of less than 10 cm (Fig. 20e).
- Airborne sedimentary plumes were observed extending from the end tip of the wind streak A (Figs. 20 and 21).

4. Discussion

4.1. Albedo type and the origin of sedimentary materials forming the wind streaks

Crater interior deposits and wind streaks include low-, intermediate-, and high-albedo sedimentary materials, all of which form smooth surfaces, dunes and rippled surfaces (Figs. 6,7,10–12). In places, intermediate-albedo deposits appear to be the result of mixing of low- and high-albedo materials (Figs. 10a and 11b). At the regional scale, the wind streaks and the low-albedo regions from which they originate are enriched in pyroxene (Poulet et al., 2008), which suggests that the low-albedo intra-crater dunes directly supply sediment to create the wind streaks (Edgett, 2002; Poulet et al., 2008).

Mass movement of light-toned deposits (Fig. 7a), extensive erosion of these materials by yardangs (Figs. 7–9) driven by aeolian abrasion by sand-sized particles (Fig. 7b), and the existence of high-albedo materials surrounding the light-toned outcrops (Fig. 6) suggest that erosion of light-toned deposits may have led to the emplacement of high-albedo surface materials. Yardangs are parallel to the propagation directions of the wind streaks that extend from the craters where the light-toned, potential source deposits are located (Figs. 8 and 9). The coincidence in the orientations is consistent with contemporaneous wind regimes scouring the light-toned outcrops and emplacing the wind streaks. These observations suggest that high-albedo sediments eroded off from intra-crater light-toned outcrops may have been transported and redeposited along the wind streaks. In addition, the formation of crater interior deposits may have also involved sedimentary particles being transported into craters from distal regions (Arvidson, 1974; Thomas, 1984) by, for example, wind streaks propagating into them (e.g., white dot in Figs. 5 and 13).

Wind streaks have been interpreted to be enriched in basaltic andesite (Bandfield et al., 2000; Hamilton et al., 2001), partly altered basalt (Minitti et al., 2002), and pyroxene (Poulet et al., 2008). Basaltic grains in the aeolian wind streaks (Geissler et al., 2008), imply a fundamental origin likely involving volcanism. In addition, if they include salts it would imply that the wind streak-forming sediments also include source materials that were produced by aqueous chemical activity somewhere in the past. Most hydrated salt minerals, however, are not hard or durable enough in terms of impact or indentation strength or brittle strength to survive abrasion in saltating environments for more than perhaps tens of kilometers transport distances. This is indicated on Earth by the rarity of dune fields made of hydrated evaporitic minerals, despite the widespread occurrence of evaporates at the surface in some regions; and where hydrated evaporite-sourced dunes occur, such as the famous gypsum dunes of White Sands, New Mexico, sources are located only a few kilometers away (Szynkiewicz et al., 2010-this issue). Even many igneous minerals (some pyroxenes and feldspars, for instance) are less hard than quartz and olivine, and could not saltate on global distance scales (Plinninger and Thuro, 2004; Rickman and Street, 2008). Among common igneous minerals, only olivine has a hardness that could enable it to survive saltation over thousands of kilometers (Plinninger

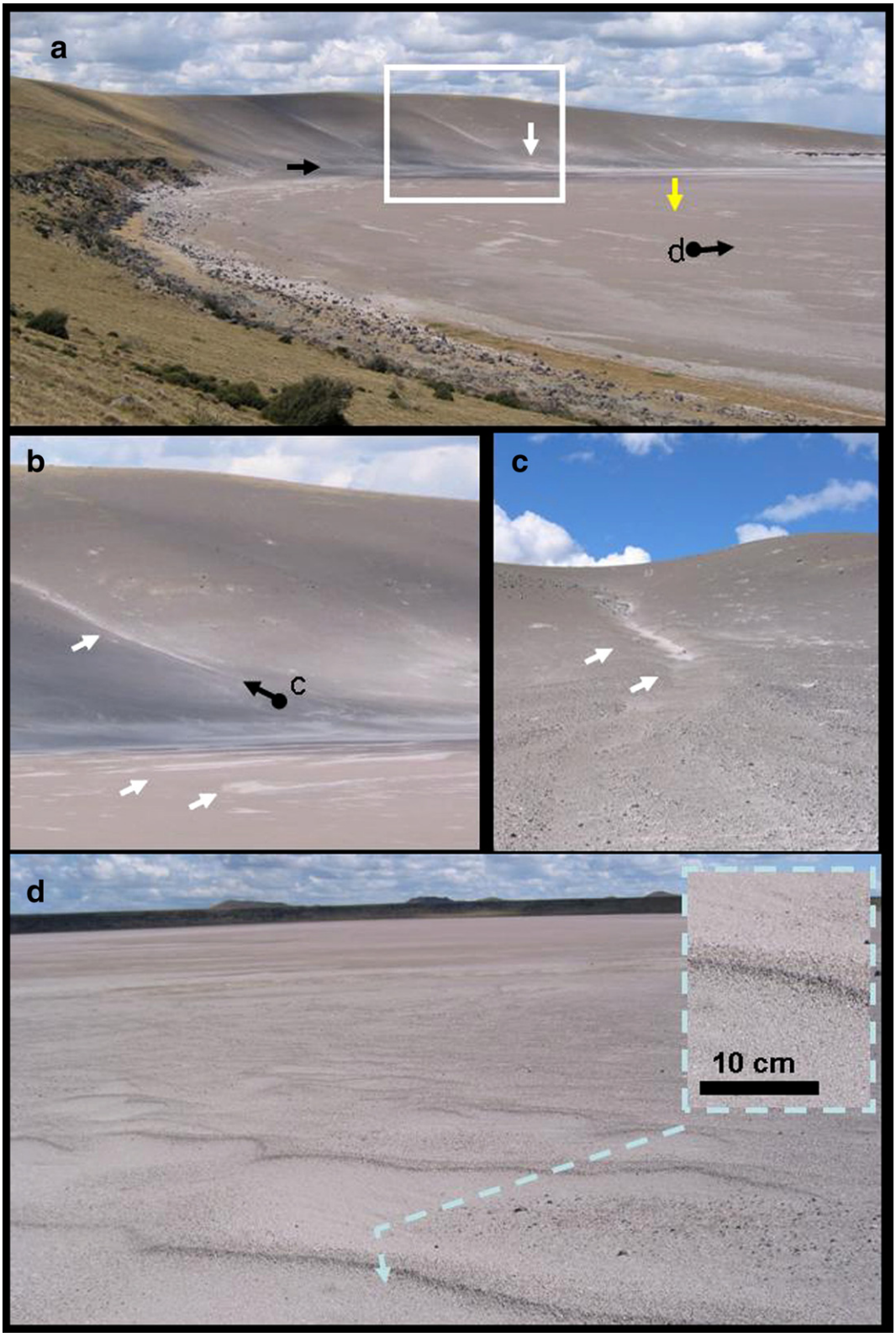

Fig. 19. (a) Eastern margin of a surveyed playa lake. (b,c and d) show close-up views.

and Thuro, 2004; Rickman and Street, 2008), but this would be possible only if a severe hydrolysis weathering environment, such as occurs on Earth, was absent which would drive the formation of relatively lower hardness phyllosilicates (Krauskopf, 1979; Moon and Jayawardane, 2004). Thus, we consider a local or regional source far more likely than anywhere outside the region of the wind streaks. Similarly, in Pali Aike wind streaks source from craters that contain low-, intermediate-, and high-albedo surface sediments. The wind streaks and the sediments in the source regions include evaporitic and volcanic geologic materials, and we have identified no wind

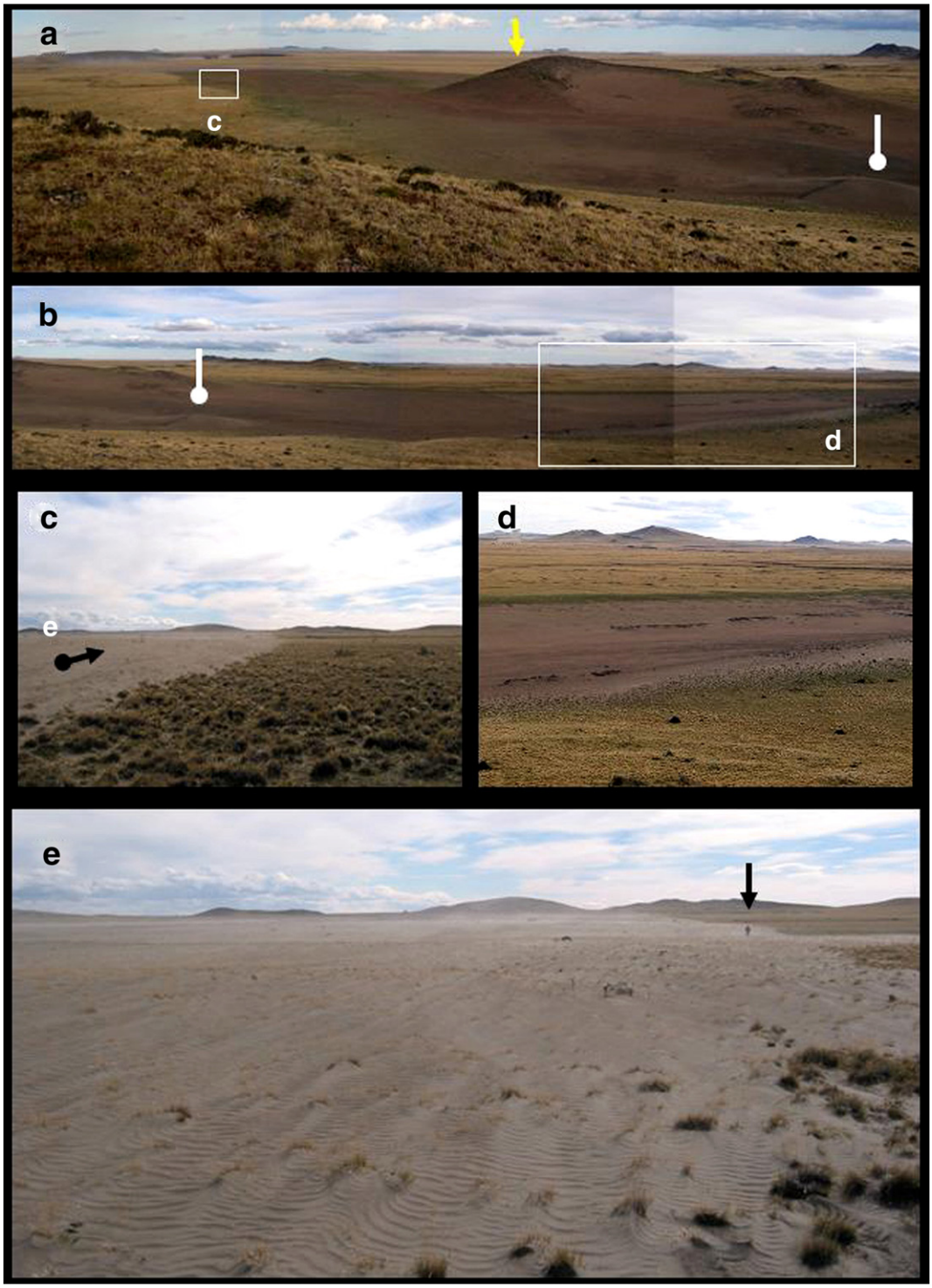

Fig. 20. (a) Looking east from the mid-section of the wind streak. (b) Looking west from the mid-section of the wind streak. (c) Close-up on panel a shows a view looking west from the end section of the wind streak. (d) Close-up on panel b shows a view looking west from the mid-section of the wind streak. (e) Close-up on panel c shows a view looking west from the end section of the wind streak. Black arrow shows a person for scale.

streak, a wind streak source region, which does not contain both types of geologic materials.

These observations suggest that the initiation and propagation of wind streaks in western Arabia Terra may have involved the mobilization and deposition of volcanic and evaporitic sediments. Physical and chemical break-down, and/or dehydration, of evaporitic sediments, however, may have led the preferential removal of hydrated minerals.

4.2. Evidence for saltation of sand-sized particles within crater interiors and wind streak surfaces on the inter-crater plains

The formation of aeolian dunes and ripples, as well as the formation of yardangs, requires the transportation of sand-sized material by saltation (Breed et al., 1989; Cutts and Smith, 1973; McCauley et al., 1977). The existence and mobility of sand-sized particles within crater interior deposits is consistent with the presence of yardangs in

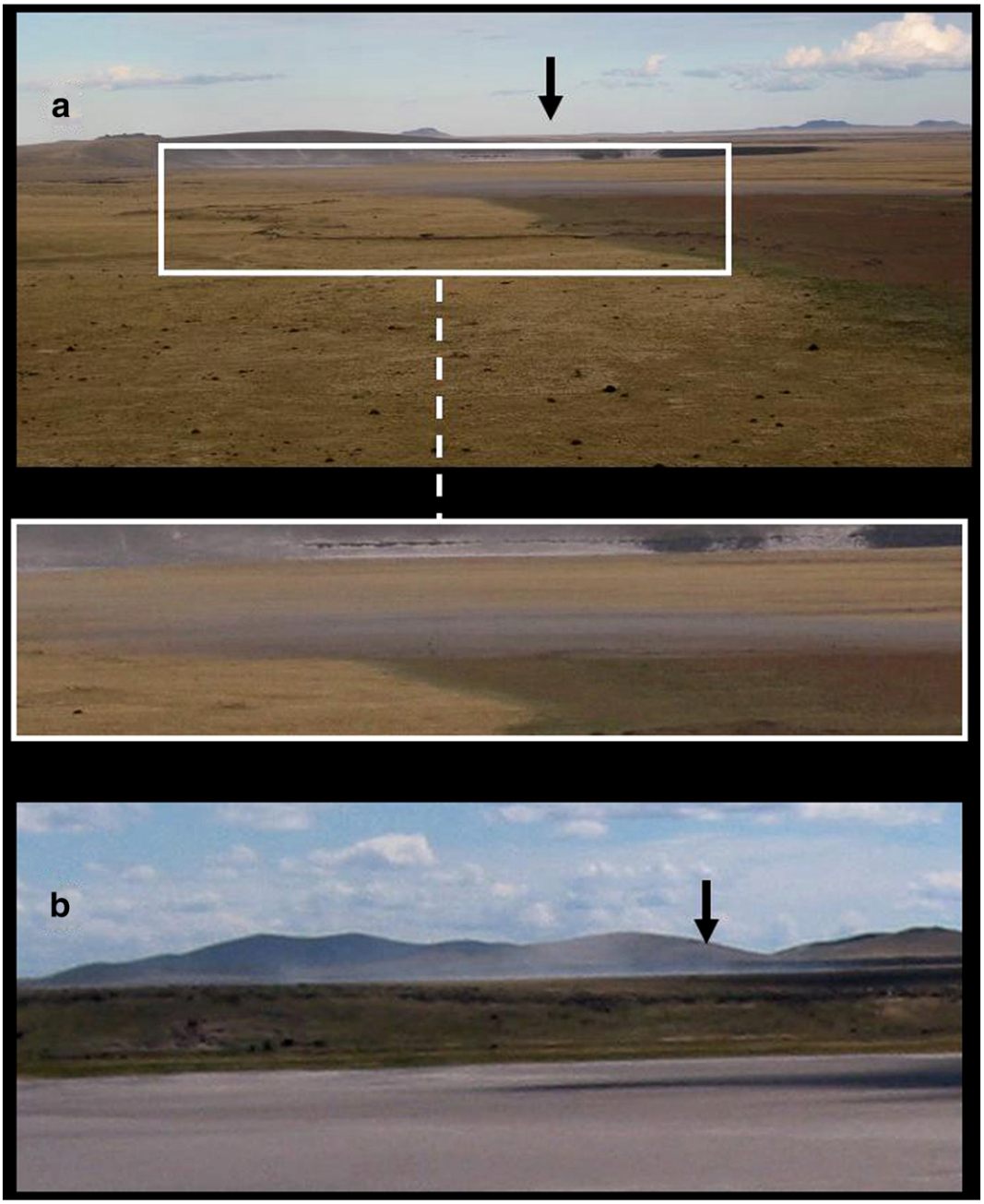

Fig. 21. Haze over the downwind end of the wind streak. (a) View from west of the wind streak. (b) View east of the wind streak from within the eastern margin of the playa.

light-toned outcrops (Figs. 8 and 9), as well as low-albedo barchan dunes, high-albedo ripples, and intermediate-albedo smooth materials embaying the ripples forming crater floor materials (Fig. 11c). Similarly, sand-sized particles are inferred to exist in the sedimentary deposits that make up the surfaces of the Rutherford (Fig. 10) and Marth wind streaks (Figs. 11 and 12). These terrains contain linear dune-like structures of intermediate-albedo (Fig. 10c), intermediate- and high-albedo transverse dunes (Figs. 10d and 12c, respectively), high-albedo barchanoid dunes (Fig. 12d), high- and low-albedo rippled surfaces (Fig. 12c and e), aeolian-scoured surfaces (Fig. 10e), and embayed terrains (Figs. 10f,12c, and white dot in 12d).

Additional evidence that indicates that wind streaks may contain a significant proportion of sand-sized sediments includes the observation that the orientation of a wind streak partly adjusts to the topography where it propagates into an impact crater (Fig. 13d). Sedimentary migration by saltation and traction, rather than airfall from dust plumes, does follow the surface topography. The topography of impact craters has been modeled to affect regional wind-flow fields (Rafkin and Michaels, 2003; Spiga et al., 2008). For example, cooling by radiation of air masses along impact crater rims may produce katabatic winds flowing down impact crater walls (Rafkin and Michaels, 2003; Geissler et al., 2008). The effect of such winds may have also contributed to or resulted in the change in orientation of the wind streak at the crater rim.

In summary, crater interior layered deposits and the wind streaks that emerge from them likely contain sand-sized sediment. Some apparent diffuse streaks appear to consist of variations in the relative coverage by high- and low-albedo aeolian dune and ripple materials (Fig. 12), rather than because of lateral gradational fading of optically thin dust veneers as once was a popular interpretation (e.g., Thomas et al., 1984). This conclusion is in agreement with previous work (Zimbelman, 1986; Edgett, 2002; Bourke et al., 2004).

Overall it seems that darker bedforms embay, and/or rest on top of, brighter ones (e.g., white dot in Fig. 10f, white arrow in Figs. 11c, 12fc and d). The high surface albedo of some dunes has been interpreted from a cover of high-albedo dust (Geissler et al., 2008). In Fig. 12g, the surface of a bright dune, however, is shown where surface gouges also display a high-albedo, suggesting that perhaps, at least in some cases, the bright sedimentary materials may consist of sand-sized particles.

In Pali Aike, the visited intra-crater playa, from which a wind streak initiates, includes rippled surfaces. Similarly, the visited wind streak include widespread ripples, and in one location, a dune. These observations indicate that the initiation and propagation of wind streaks in this region involved the migration and emplacement of sand-sized particle.

4.2.1. Evidence for sedimentary migration out of craters via saltation

Suspension from within the crater interior deposits may have played an important role in transporting sediments into the wind streaks (Edgett, 2002). We find that a train of aeolian bedforms, as well as aeolian erosion landforms, how extend to and over the rim of the Rutherford impact crater (Fig. 10b). These observations are consistent with the propagation of sand-sized particles from within the crater up the wind-facing crater wall and onto the wind streak. In another location, we observe the extension of dunes within an impact crater upslope and across a crater rim on the margin of Planum Boreum (Fig. 3). Thus, saltation and traction are at least a factor in the transport of grains from crater interiors across topographic barriers, which is consistent with results obtained through terrestrial field studies of wind streaks (Zimbelman et al., 1995; Zimbelman and Williams, 2002) and with our observations in Pali Aike of sedimentary bedforms extending up along wind-facing slopes and onto associated wind streaks.

4.3. Low mobility of high-albedo aeolian landforms

High-albedo bedforms are commonly embayed by darker ones, suggesting that they are more difficult to mobilize by wind activity. This observation could be explained by the encasing of sand by dust deposits (Geissler et al., 2008). Close-ups of high-albedo margins marking the margins of the wind streak extending from Marth crater (Fig. 12a and b) as well as low-albedo materials on the floor of Becquerel crater (Fig. 7e) reveal clusters of smaller wind streaks, which emanate from some of the smaller craters, and preserve multiple orientations. The crater clusters located along the margin of the Marth wind streak display wind streaks that trend E, SE, and SW, and those located in the floor of Becquerel crater display win streaks that trend W and SW. In both cases, the wind streaks trending SW are significantly more extensive than the other subsets. Both the margins of the main Marth (Fig. 12e) and Becquerel (Fig. 5) wind streaks trend SW.

Because these streaks do not appear to have been remobilized to conform to the most recent wind direction, they may be cemented and/or consist of very fine-grained electrostatically cohesive materials. Cementation would be enhanced if these materials consisted of (or contained) salts. A potential source of high-albedo salts could be the light-toned outcrops that contain hydrated mineral (Poulet et al., 2008), interpreted to have a lacustrine origin (Malin and Edgett, 2000; Crowley et al., 2008).

Similarly, in Pali Aike some wind streaks have high-albedo halos, which appear to consist of predominantly dolomitic sands, which most likely were eroded from the playas from which they source. In one instance, a high-albedo margin is preserved as the outline of a wind streak, which has otherwise undergone extensive dissipation. This arrangement is consistent with relatively enhanced sedimentary induration, perhaps from dolomite cementing the surface (Anand et al., 1997). We propose that in Arabia Terra high-albedo materials may contain, and/or consist of salt minerals. Whenever surface temperatures are at least at the eutectic melting point of ice-salt mixtures (Brass, 1980; Marion et al., 2003; Kargel and Marion, 2004), or when a peritectic incongruent melting point is reached under humid conditions (Brass, 1980; Marion et al., 2003; Kargel and Marion, 2004), the high-albedo sediments may become cemented, and, therefore, be less likely to be mobilized by saltating sands.

We note that water activities corresponding to relative humidities of a few percent (relative to the vapor pressure of ice) are sufficient to stabilize some hydrated salts such as kieserite (Feldman et al., 2004). This hypothesis could explain the apparent low mobility of high-albedo dune forms by the creation of cements and duricrust by either aqueous precipitation or atmospheric driven hydration (Marion et al., 2003; Vaniman and Chipera, 2006; Marion et al., 2007).

Even a trace amount of salts is sufficient to form weak crusts when dry or frozen (Cooper and Mustard, 2002); or deliquescent salts could produce traces of liquids and form damp, cohesive silts when heated or when the humidity rises (Kargel, 2004). Thus, salt-bearing sands or silts could become stabilized by either cementation or incongruent melting of hydrated salts, whereas mechanical breakup and destabilization of crusts could occur by freeze–thaw, heating/cooling, or impacts of saltating grains, thus rendering the sediments prone to further saltation. Eutectic melting/freezing or peritectic dissociation/hydration, like the melting point of ice, all being thermally invariant processes, can occur suddenly and consolidate an entire sediment surface in a brief time. Unlike the melting of ice, which generally does not occur on Mars (either because it is too cold or because it is too dry where the temperature is warm enough), some salt assemblages can melt and remain liquid (the relative humidity being high enough to stabilize the low-temperature, low water-activity liquid phase) at times under the present Martian climatic regime.

4.3.1. Origin of high-albedo halos around wind streaks

The origin of the high-albedo halos that surround wind streaks in western Arabia Terra (e.g., Fig. 2) has been an issue of debate for the past three decades. Models invoked for formation include: (1) saltating sand mobilizes high-albedo dust and re-deposits this material along the streak margin (Thomas et al., 1981), (2) saltating sand impinges upon a crusted dust/soil along the streak margin (Mustard, 1997; Cooper and Mustard, 1998), (3) sand fines toward the margins of each streak (Thomas et al., 1981), and (4) the material comprising high-albedo margins is dust (Thomas et al., 1984). In a dust deposition model for genesis of the western Arabia wind streaks, dust would settle out of a plume of suspended fines as they are removed from the dune field and crater floor upwind of the streak (Edgett, 2002). This explanation is not entirely satisfactory, because if high-albedo dust is the last material to settle out of suspension, then it should also settle upon the low-albedo wind streaks and eventually obscure them (Edgett, 2002).

We have identified a region on the floor of Becquerel crater, where low-albedo surface materials show a high-albedo halo (Fig. 6 and 7d,e); a morphologic association identical to that observed in many wind streaks in western Arabia Terra. Here the source materials of the low-albedo surface within the crater, however, can be traced to barchan dune fields (Figs. 6 and 7). We also found that the high-albedo deposits appear to be derived, at least in part, from a large light-toned layered outcrop in the region (Figs. 6 and 7).

We suggest that it is possible that in Arabia Terra the high-albedo materials forming the margins of low-albedo deposits in wind streaks, and within interior crater deposits, may be enriched in evaporitic minerals, leading to their cementation and fixation to the surface. Given that materials cemented by salts may be preferentially preserved around the margin of low-albedo deposits may be related to a lesser extent to surface saltation associated with the migration of dark materials, which would be consistent with our observations in

Pali Aike that the visited wind streak had sharp margins (Fig. 20) and, thus, well-delimited boundaries for the paths of sand migration.

4.4. Patterns of recent wind streak activity

We observe that a wind streak propagated 10 km over a 21-year period in Arabia Terra (Fig. 11), and two wind streaks in Pali Aike that have propagated 3.5 km and 4.9 km respectively, each over a period of 4 years. In Arabia Terra (Edgett, 2002) and in Pali Aike, however, only a small subset of wind streaks display changes in shapes.

Thus, it appears that whereas aeolian processes are currently actively mobilizing sediments along wind streaks in both study areas, systems of inactive and active wind streaks co-exist within wind streak fields. If the physical and chemical (mineralogical) differences driving stabilization or destabilization are subtle, then it can be understood why one wind streak might remain stable even while another becomes unstable.

Similarly, whereas the mobilization of sand-sized sediment from dunes (Bourke et al., 2008) has been previously recognized, such events do not appear to be frequent or widespread on Mars (Edgett, 2002). Perhaps the Martian wind streak deposits are on the whole more stable than they are on Earth, and, therefore, atmospheric instabilities leading to changes in shape are less frequent.

4.5. Formation of wind streak clusters

Our results show that in western Arabia Terra the mean values for the NND of crater interior deposits are lower within the region with wind streaks when compared to the region without wind streaks (Fig. 2). In contrast, these values are similar within the regions with and without wind streaks in Pali Aike (Fig. 14). These observations suggest that, at least in the case of Arabia Terra, the formation of the wind streak cluster may have been, at least partly, a consequence of the existence of closely-spaced crater interior deposits in the region.

This proposition is in agreement with the observation that in western Arabia Terra some wind streaks extend into some impact craters located along the paths (white dot in Figs. 5 and 13). Sand grains migrating into the interior deposits of the craters could mobilize (lift) silt- and sand-sized particles through particle rebound during saltation, triggering the initiation and propagation of another wind streak in the downwind direction, and thereby promoting the emergence of wind streak clusters. In addition, the propagation of wind streaks into impact craters along the paths may have contributed to the formation, and/or growth, of interior sedimentary deposits within those craters.

In some locations we have identified extensive sedimentary deposits that consist of sequences of wind streaks and crater interior deposits occurring across the cratered highlands. We refer to these as paths of high sedimentary transfer (Fig. 22). We propose that, at least in western Arabia Terra, in addition to being zones of extensive deposition, these paths of high sedimentary transfer are (or have been) zones of significant surface erosion. Surface erosion associated with the propagation of wind streaks in these regions (e.g., Figs. 9b and 10e) may have increased the volume of sediments at regional scales, which would in turn become available as potential source materials for wind streaks and crater interior deposits.

On the other hand, whereas in Pali Aike we have not observed wind streaks propagating into craters aligned in the downwind direction, airborne sedimentary plumes were observed extending from the end tip of a wind streak, approximately 2 km west of a playa crater (wind streak A in Figs. 20 and 21). Therefore, it is possible that in Pali Aike too sedimentary transfer has occurred from wind streaks to crater interior deposits from which other wind streaks initiate.

Our observations suggest that in western Arabia Terra and in Pali Aike, wind streaks cluster in zones where a higher occurrence of relatively deeper craters occur. Deeper craters would produce higher intensity katabatic and anabatic (upslope) thermal winds (Rafkin and Michaels, 2003; Geissler et al., 2008), capable of enhancing sedimentary migration into and out of the craters, respectively. Global Circulation Models (GCM) surface winds predict an increase of wind speeds in western Arabia Terra (Fenton and Richardson, 2001), an effect that may be enhanced by, or resulted from, the effect of regional thermal circulations related to the presence of deeper craters (Rafkin and Michaels, 2003). Greater crater diameters would imply larger areas for sedimentary accumulation into crater interior deposits. Our results show, however, no significant difference in the diameters of craters located in regions with and without wind streaks in Arabia Terra and Pali Aike.

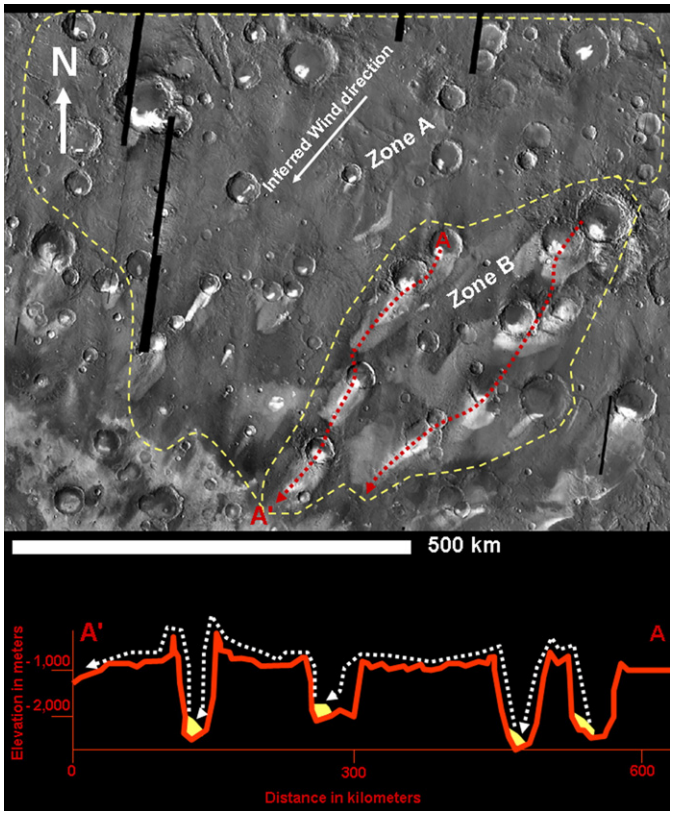

Fig. 22. (a) Part of western Arabia Terra showing two areas of wind streak occurrence. In Zone A, most wind streaks do not extend into craters in the downwind direction. In Zone B, most wind streaks extend into craters in the downwind direction. We refer to these interconnected systems of wind streaks as paths of high sedimentary transfer (dotted red lines). (b) MOLA derived elevation profile A–A' (red line). The yellow areas show the locations of crater interior deposits. The dotted white lines show the zone interpreted as a path of high sedimentary transfer.

On the other hand, within the region where impact craters interior deposits are less abundant and more distantly spaced (Fig. 2), sedimentary transfer along wind streaks may not comprise an efficient mechanism to form, supply, and/or mobilize sedimentary deposits within impact craters in the downwind direction (Fig. 22). Edgett (2002) shows that impact craters within this region, which have low-albedo interior deposits but lack associated wind streaks, also mostly lack interior dune fields. This is consistent with our hypothesis, which suggests that these craters would receive relatively lower volumes of sediments transported via surface saltation.

In summary, we suggest that the likelihood of wind streak clusters developing in a given region may directly correlate how frequently wind streaks extend from the source craters to other craters aligned in the downwind direction, which in turn will directly correlate to increasing inter-crater proximity as well as to increasing crater areal density. In addition, the formation of wind streak clusters appears to have also been associated with the presence of relatively deeper craters in the regions of study.

5. Conclusions

This investigation allows the following conclusions to be drawn:

(1) Our observations indicate that in western Arabia Terra and in Pali Aike, the formation of wind streak clusters has been at least partly controlled by relatively high areal densities of closely-spaced craters containing evaporitic and lithic interior sedimentary deposits. An additional potential controlling factor on the formation of these clusters is the presence within them of populations of craters that are deeper and larger than those in surrounding terrains.
(2) Wind streaks initiate at crater interior deposits, which include high-albedo outcrops of possible lacustrine origin (Poulet et al., 2008) for Arabia Terra and evaporites for Pali Aike, suggesting that the composition of the source materials forms an important constraint for the formation of wind streaks.
(3) Crater interior deposits and wind streaks include aeolian bedforms of varying albedo, which suggests that wind streaks have a sand-sized component that may be significant in this region.
(4) Whereas high- and low-albedo sediments display bedforms, the latter appear more readily mobilized than the former as indicated by embayment and superposition relationships.
(5) The transport of crater interior deposits into the wind streaks involved, at least in some cases, saltation and traction of sand-sized sediments along downwind crater slopes.
(6) The interiors of impact craters in western Arabia Terra include extensively eroded surfaces, which indicate active saltation in the direction of the emergent wind streaks. Thus, in addition to intra-crater low-albedo barchan dune fields and sediments produced by erosion of outcrops within the impact craters, we suggest that an additional source of sediments for wind streaks is from upwind streaks propagating from upwind craters.
(7) The high-albedo halos around wind streaks in western Arabia Terra appear to consist of materials compositionally different from the low-albedo materials.
(8) We have observed recent propagation of a wind streak that appears to have involved migration by surface saltation.

6. Directions of future research

Important science issues regarding the formation of wind streaks in western Arabia Terra and in Pali Aike, revealed through this investigation, remain poorly understood and may become the focus of future research:

1. It remains unclear why all craters that contain sand-sized sedimentary deposits in a given region do not produce wind streaks. The fact that the wind streaks cluster is in a zone where most impact craters contain layered interior deposits hints at (but does not prove) a morphogenetic association in which wind streaks preferentially develop where barchan dunes can supply sand and erode interior light-toned outcrops to produce high-albedo deposits. A possibility is that the light-toned layered deposits contain sufficient amounts of salts such that the erosion led to the mixing of salt grains and basaltic sediments. In situ geologic studies reveal that salts form key components in some aeolian deposits, for example in dunes studied by the Mars Exploration Rover Opportunity (Squyres et al., 2004; Clark et al., 2005). Furthermore, part of the northern circumpolar erg has been found by analysis of Mars Express OMEGA data to contain abundant gypsum and hydrated sulfates (Langevin et al., 2005). We propose that inter-particle abrasion within migrating sand sheets would have led to a relatively rapid breakdown of sand-sized salt grains into silt- and dust-sized particles. Zones in the wind streak that became silt-enriched would have gained stability from the higher threshold of wind shear stress required for mobilization (Greeley and Iversen, 1985). The ultra-rough microtexture of (1) partially dissolved/etched salt surfaces and (2) sedimentary deposits played a significant role in initiating sand traps by limiting saltation and creating pockets of accumulated sand patches capable of absorbing momentum of incoming grains (Greeley and Iversen, 1985), similar to the mechanism involved in the initiation of proto-dunes (Bagnold, 1941). In addition, the impacting grains could help to shelter the surface grains from subsequent saltation impact, thereby increasing the stability of the bulk sedimentary deposit.
2. The degree of variability in regional wind patterns in western Arabia Terra remains unclear. For example, in addition to the radial systems of streaks shown in Fig. 10f, we have identified yardangs that extend from the floor of a crater and along its upwind margin (Fig. 8). These yardangs represent saltation into and/or out of the crater (e.g., Fig. 11). In the latter case, they would have formed during a period of reversed wind direction relative to that indicated presently by the orientation of the wind streaks. Also, the dashed arrow in Fig. 7 shows the margin of a streak that propagates at an angle of about 10 ° from the orientation of the yardang systems. Variable wind directions in the region may have led to the dispersion of sediments other than that indicated by the main wind streak systems during time spans extending from the formation of the yardangs to the emplacement of the wind streaks.
3. It remains unclear why only a subset of wind streaks within the western Arabia and Pali Aike clusters appear to have undergone propagation. We speculate that instabilities may be prone to develop where more extreme conditions occur in relevant aspects such as the composition and texture of the materials and local topography. Also, random geologic (e.g., impacts) and atmospheric events may also create episodic, localized instabilities.
4. It remains unclear why in western Arabia Terra and in Pali Aike regions where crater interior deposits show relatively lower areal densities that wind streaks do not tend to develop. We speculate that in these regions interior deposits may be more likely to become cemented by duricrust formation, which has been common for soils in the case of Mars (Squyres et al., 2004; Clark et al., 2005). Duricrusts may particularly develop in areas where a sustained influx of sedimentary particles does not occur (Kieffer et al., 1981; Presley and Arvidson, 1988; Arvidson et al., 1989; Christensen and Moore, 1992; Mustard, 1997).

Further studies of wind streaks in Pali Aike could improve our understanding on how wind streaks in Arabia Terra initiate, propagate and vanish, as well as on the nature of the bright halos that many of them display.

Acknowledgements

We would like to thank three anonymous reviewers whose comments greatly improved this manuscript. We are also grateful to Mary Bourke for her insightful discussions and editing. We also thank Scott Stanley for his in-depth revision of this manuscript. Finally, we thank Martin Koss for field guidance in the Pali Aike region of southern Argentina.

Appendix A

Table 1
Wind streak widths and lengths in meters for Arabia Terra.

Length	Width	L/W
133251.6	107619.6	1.238171
169852.9	63486.55	2.675415
228360.5	87949.27	2.596502
66935.72	90866.32	0.736639
61288.93	46097.68	1.329545
22940.14	16250.16	1.411687
15147.12	9086.455	1.667
26166.02	11453.94	2.284456
28474.12	29363.24	0.96972

Table 1 (*continued*)

Length	Width	L/W
45647.72	22972.03	1.987101
57435.91	53839.88	1.066791
24882.75	25016.01	0.994673
56711.24	15214.84	3.727362
36131.43	32126.67	1.124655
86097.44	76682.47	1.122779
152627.3	88419.09	1.726181
60025.56	74286.04	0.808033
121178.7	134572.6	0.900471
36758.13	49035.31	0.749626
84025.97	55277.59	1.520073
54111.1	20757.2	2.606859
67286.8	48698.44	1.381703
71667.05	49050.15	1.461097
115782.5	69418.63	1.667887
70588.73	38728.17	1.822672
47249.72	24358.07	1.939798
58627.66	36101.95	1.623947
91755.29	44497.76	2.06202
48572.15	20923.85	2.321377
48165.87	10184.48	4.729339
20594.05	8018.56	2.568298
15390.43	6307.888	2.439871
27852.95	32916.11	0.84618
20526.88	16869.99	1.216769
45238.94	21565.61	2.097735
44416.85	34678.66	1.280812
46036.05	23330.33	1.973228
57351.33	60789.32	0.943444
23366.22	15737.1	1.484786
20154.55	10019.25	2.011582
9052.316	4528.748	1.998856
176573.1	81730.83	2.160422
42772.45	11175.05	3.827496
61560.85	15175.55	4.056582
37884.6	19669.48	1.92606
39116.94	22241.77	1.758715
71951.99	43390.94	1.658226
55691.93	31607.94	1.76196
117940.2	19704.87	5.985334
78742.77	80381.48	0.979613
165468.7	83786.5	1.974885
31654.81	16608.09	1.905987
14486.1	14659.65	0.988161
106592.6	54287.71	1.963476
51084.3	50106.73	1.01951
115938.8	46658.38	2.484843
125484.7	44374.44	2.82786
48629.03	33888.66	1.434965
89706.67	76703.68	1.169522
19000.54	22585.08	0.841288
84854.31	45382.83	1.869745
82577.9	58724.18	1.406199
73583.43	30582.76	2.406043
26066.49	16822.63	1.549489
65202.01	41717.55	1.562939
57594.11	47917.49	1.201943

Table 2
Crater interior deposits nearest-neighbor distance in meters for Arabia Terra.

Region with wind streaks	Region with no wind streaks
103350	79939.78
47407.28	80176.36
37548.13	162237.4
86982.22	60780.84
103501.9	59383.55
88745.25	71026.45
81188.23	170619.5
76312.14	188209.8
78095.81	237445.5
112345	95890.25
79614.32	93496.69
72799.77	102736.5
75809.95	162519.5

Table 2 (*continued*)

Region with wind streaks	Region with no wind streaks
70154.02	65810.29
109311.4	65213.97
201594.5	113965
151092.7	69045.6
173887.8	71098.36
128816.6	88060.38
114588.5	103761.2
50794.17	233794.7
55383.34	235305.1
38752.19	277265.9
40587.9	676019.3
70838.04	140737.9
116031.4	128410.4
152178.4	85757.96
96290.85	43355.8
75088.18	138541.5
170245.6	59659.69
176310.9	59619.52
113482.6	25640.3
91169.27	21050.74
89923.6	22944.05
45736.37	50696.23
74072.01	42243.65
29263.57	103012.3
29630.32	112720.8
63482.08	210410.8
75266.65	
78981.29	
73587.16	
114699.1	
124814.5	
36979.11	
37035.57	
99100.93	
28956.4	
31072.47	
71500.66	
82111.74	
63591.18	
65625.22	
65943.77	
142291.6	
56629.51	
53568.16	
71856.31	
293445.3	
99060.79	
101032.3	
156199.2	
138903.8	
124478.6	
104225.8	
102125	
89332.68	
89332.68	

Table 3
Measurements of crater diameters and depths in meters for Arabia Terra.

Region with wind streaks		Region with no wind streaks	
Diameter	Depth	Diameter	Depth
57863.82	557.2545	43944	211.7081
76079.28	1043.341	90340.66	455.745
113128.9	1884.841	138756.9	833.3825
174565	2983.986	43395.99	280.9885
158739.8	2718.943	196519.8	1490.646
121367.8	2112.874	159668.5	1255.68
90154.87	1596.593	96882.78	839.6381
84520.19	1685.097	76709.64	672.4437
116406.8	2320.986	81425.23	719.4265
68266.3	1409.922	62113.42	787.5146
98900.56	2115.389	43909.23	671.651
33645.54	746.346	104060.5	1615.815
68266.3	1612.344	79762.04	1267.5

(*continued on next page*)

Table 3 (*continued*)

Region with wind streaks		Region with no wind streaks	
Diameter	Depth	Diameter	Depth
42082.35	1062.689	52638.42	883.2244
94272.52	2397.434	111287.6	1879.209
66560.65	1702.519	88845.16	1528.752
67657.77	1748.214	79834.26	1376.43
61778.44	1625.706	33809.98	583.4018
73493.43	1988.942	108147.7	1919.097
42265.09	1188.454	59752.73	1082.335
94108.24	2689.467	112216.4	2034.943
60016.95	1768.874	66098.73	1213.316
42678.72	1261.028	40444.4	776.0023
39532.86	1176.016	77718.59	1497.674
51366.38	1541.834	46935.9	910.6725
33292.01	1002.36	63607.9	1234.643
64368.66	1941.403	36455	755.8355
34883.24	1072.826	65611.62	1373.137
88442.63	2731.777	114126.6	2410.26
40573.02	1265.246	91833.21	1946.453
90409	2835.635	42900.36	916.5556
48111.49	1519.407	58549.74	1415.576
65462.51	2099.548	53989.04	1315.941
45277.7	1453.133	46431.45	1133.345
45420.53	1516.867	137563	3358.573
59612.23	2057.998	48449.27	1193.133
31816.97	1105.326	45422.55	1148.31
62970.53	2387.911	54026.75	1378.507
27964.24	1067.806	49975.4	1276.782
54647.86	2092.747	49343.93	1312.328
36431.91	1450.865	66319.21	1782.103
63078.47	2597.191	54197.9	1470.603
38359.16	1640.817	89828.9	2490.587
36212.91	1594.608	67629.38	1911.541
48111.49	2362.12	57576.33	1637.172
41093.11	2072.494	71144.43	2050.994
51366.38	2664.578	28778.21	860.0746
34378.91	1895.748	38350.67	1150.862
48652.11	2762.293	19704.11	613.0435
27072.6	1548.96	39889.8	1248.303
		19180.31	619.71
		48441.39	1578.112
		83729.86	2728.056
		30795.34	1035.638
		52562.58	1781.893
		50708.15	1745.324
		58027.79	2091.526
		79914.85	2899.857
		58475.97	2152.63
		54026.75	2012.06
		45915.91	1754.054
		49512.22	2324.752
		34325.63	1857.508

Table 4
Wind streak widths and lengths in meters for Patagonia.

Length	Width	l/w
730	770	0.94805
1130	830	1.36145
1500	950	1.57895
2160	1160	1.86207
1850	880	2.10227
2080	870	2.3908
800	310	2.58065
710	240	2.95833
5990	1330	4.50376
8460	1760	4.80682
8500	1060	8.01887

Table 5
Crater interior deposits nearest-neighbor distance in meters for Patagonia.

Region with no wind streaks	Region with wind streaks
1230	1310
1610	1620

Table 5 (*continued*)

Region with no wind streaks	Region with wind streaks
1660	1720
1810	1750
1960	2270
2440	3030
2510	3140
3030	3790
3310	5330
3540	6180
3590	6480
3750	
4220	
5200	
5920	
6090	

Table 6
Measurements of crater diameters and depths in meters for Patagonia.

Region with wind streaks		Region with no wind streaks	
Diameter	Depth	Diameter	Depth
1713	42	1668	37
1845	49	1810	35
3996	51	3207	85
2756	40	2413	80
1439	83	2604	54
2829	58	1046	22
2387	109	1134	33
1734	42	2352	61
1449	34	2045	55
1560	28	2591	47
		2608	34
		2265	39
		1124	13
		925	27

References

Anand, R.R., Phang, C., Wildman, J.E., Lintern, M.J., 1997. Genesis of some calcretes in the southern Yilgarn Craton, Western Australia: implications for mineral exploration. Australian Journal of Earth Sciences: An International Geoscience Journal of the Geological Society of Australia 1440–0952 44 (1), 87–103.

Arvidson, R.E., 1974. Wind-blown streaks, splotches, and associated craters on Mars: statistical analysis of Mariner 9 photographs. Icarus 21 (1), 12–27.

Arvidson, R., Guinness, E., Dale-Bannister, M., Adams, J., Smith, M., Christensen, P.R., Singer, R.B., 1989. Nature and distribution of surficial deposits in Chryse Planitia and vicinity, Mars. Journal of Geophysical Research 94 (B2), 1573–1587.

Bagnold, R.A., 1941. The Physics of Blown Sand and Desert Dunes. Chapman and Hall, London.

Baker, V.R., 1982. The Channels of Mars. University of Texas Press, Austin. 198 pp.

Bandfield, J.L., Hamilton, V.E., Christensen, P.R., 2000. A global view of Martian surface compositions from MGS-TES. Science 287 (5458), 1626.

Baruth, B., Endlicher, W., Hoppe, P., 1998. Climate and desertification processes in Patagonia. Bamberger Geographische Schriften 15, 307–320.

Basile, I., Grousset, F.E., Revel, M., Petit, J.R., Biscaye, P.E., B., N.I., 1997. Patagonian origin of glacial dust deposited in East Antarctica (Vostok and Dome C) during glacial stages 2, 4 and 6. Earth and Planetary Science Letters 146, 573–589.

Bourke, M.C., Bullard, J.E., Barnouin-Jha, O.S., 2004. Aeolian sediment transport pathways and aerodynamics at troughs on Mars. Journal of Geophysical Research 109 (E07005). doi:10.1029/2003JE002155.

Bourke, M.C., Edgett, K.S., Cantor, B.A., 2008. Recent aeolian dune change on Mars. Geomorphology 94, 247–255.

Brass, G.W., 1980. Stability of brines on Mars. Icarus 42, 20–28.

Breed, C.S., McCauley, J.F., W., M.I., 1989. Wind erosion forms. In: Thomas, D.S.G. (Ed.), Wind erosion forms. In arid zone geomorphology. InHalstead Press, New York, pp. 284–307.

Carr, M.H., 1996. Water on Mars. Oxford University Press, New York. 229 pp.

Christensen, P.R., Moore, H.J., 1992. The Martian surface layer. In: Kieffer, H.H. (Ed.), Mars, pp. 686–729.

Christensen, P.R., Anderson, D.L., Chase, S.C., Clark, R.N., Kieffer, H.H., Malin, M.C., Pearl, J.C., Carpenter, J., Bandiera, N., Brown, F.G., Silverman, S., 1992. Thermal emission spectrometer experiment: Mars Observer mission. JGR 97 (E5), 7719–7734.

Christensen, P.R., Bandfield, J.L., Smith, M.D., Hamilton, V.E., Clark, R.N., 2000. Identification of a basaltic component on the Martian surface from Thermal Emission Spectrometer data. Journal of Geophysical Research 105 (E4), 9609–9621.

Christensen, P.R., Bandfield, J.L., Hamilton, V.E., Ruff, S.W., Kieffer, H.H., Titus, T.N., Malin, M.C., Morris, R.V., Lane, M.D., Clark, R.L., Jakosky, B.M., Mellon, M.T., Pearl, J.C., Conrath, B.J., Smith, M.D., Clancy, R.T., Kuzmin, R.O., Roush, T., Mehall, G.L., Gorelick,

N., Bender, K., Murray, K., Dason, S., Greene, E., Silverman, S., Greenfield, M., 2001. Mars Global Surveyor Thermal Emission Spectrometer experiment: investigation description and surface science results. JGR 106 (E10) 23,923–23,871.
Clark, B.C., Morris, R.V., McLennan, S.M., Gellert, R., Jolliff, B., Knoll, A.H., Squyres, S.W., Lowenstein, T.K., Ming, D.W., Tosca, N.J., 2005. Chemistry and mineralogy of outcrops at Meridiani Planum. Earth and Planetary Science Letters 240 (1), 73–94.
Cooper, C.D. and Mustard, J.F., 1998. Rates of Erosion in Oxia Palus, Mars. LPSC XXIX. Abstract No.1164.
Cooper, C.D., Mustard, J., 2002. Spectroscopy of loose and cemented sulfate-bearing soils: implications for duricrust on Mars. Icarus 158 (1), 42–55.
Corbella, H., 2002. El campo volcano-tectónico de Pali Aike. In: Haller, M.J. (Ed.), Geología y Recursos Naturales de Santa Cruz, Relatorio de XV Congreso Geológico Argentino, El Calafete Buenos Aires, pp. 287–303.
Corbella, H., Chelotti, L., 1998. Pali-Aike tectono-volcanic field: modern Maars on a rejuvenated Jurassic Rift, Southern Patagonia. IAVCEI International Volcanological Congress. Cape Town- South Africa: Abstracts, p. 14.
Crowley, J., Hook, S., Bridges, N., Thomson, B., Baldridge, A., Brown, A., De Souza Filho, C.R., Marion, G., Kargel, J., 2008. Lacustrine sedimentary rocks from an alkaline environment in Becquerel Crater, Arabia Terra, Mars. Joint Meeting of The Geological Society of America, p. 195–11.
Cutts, J.A., Smith, R.S.U., 1973. Eolian deposits and dunes on Mars. Journal of Geophysical Research 78, 4139–4154.
Edgett, K.S., 2002. Low-albedo surfaces and eolian sediment: Mars Orbiter Camera views of western Arabia Terra craters and wind streaks. Journal of Geophysical Research 107 (E6), 10.1029.
Edgett, K.S., Malin, M.C., 2000. New views of Mars eolian activity, materials, and surface properties: three vignettes from the Mars Global Surveyor Mars Orbiter Camera. Journal of Geophysical Research 105 (E1), 1623–1650.
Feldman, W.C., Mellon, M.T., Maurice, S., Prettyman, T.H., Carey, J.W., Vaniman, D.T., Bish, D.L., Fialips, C.I., Chipera, S.J., Kargel, J.S., Elphic, R.C., Funsten, H.O., Lawrence, D.J., Tokar, R.L., 2004. Hydrated states of $MgSO_4$ at equatorial latitudes on Mars. Geophys. Res. Lett. 31 (16), L16702. doi:10.1029/2004GL020181.
Fenton, L.K., Richardson, M.I., 2001. Martian surface winds: insensitivity to orbital changes and implications for aeolian processes. Journal of Geophysical Research 106 (E12), 32,885–32,902.
Geissler, P.E., Johnson, J.R., Sullivan, R., Herkenhoff, K., Mittlefehldt, D., Fergason, R., Ming, D., Morris, R., Squyres, S., Soderblom, L., Golombek, M., 2008. First in situ investigation of a dark wind streak on Mars. Journal of Geophysical Research 13 (E12S31). doi:10.1029/2008JE003102.
Gonzalez, L., Rial, P.E., 2004. Guia geografica interactiva de Santa Cruz, Rio Gallegos. 59 pp.
Greeley, R., 1986. Aeolian landforms: laboratory simulations and field studies. Aeolian Geomorphology. Allen and Unwin, Winchester, Mass. 195–211 pp.
Greeley, R., Iversen, J.D., 1985. Wind as a Geological Process on Earth, Mars, Venus, and Titan. Cambridge Univ. Press, New York. 333 pp.
Greeley, R., Thompson, S.D., 2003. Aeolian features and wind predictions at the Terra Meridiani and Isidis Planitia potential Mars Exploration Rover landing sites. Journal of Geophysical Research 108 (E12), 8093. doi:10.1029/2003JE002110.
Greeley, R., Christensen, P., Carrasco, R., 1989. Shuttle radar images of wind streaks in the Altiplano, Bolivia. Geology 17 (7), 665–668.
Greeley, R., Iversen, J.D., Pollack, J.B., Udovich, N., White, B., 1974a. Wind Tunnel Simulations of light and dark streaks on Mars. Science 183 (4127), 847–849.
Greeley, R., Iversen, J.D., Pollack, J.B., Udovich, N., White, B., 1974b. Wind tunnel studies of Martian aeolian processes. Proceedings of the Royal Society of London. Series A, Mathematical and Physical Sciences (1934–1990) 341 (1626), 331–360.
Hamilton, V.E., Wyatt, M.B., McSween Jr., H.Y., Christensen, P.R., 2001. Analysis of terrestrial and Martian volcanic compositions using thermal emission spectroscopy: 2. Application to Martian surface spectra from the Mars Global Surveyor Thermal Emission Spectrometer. J. Geophys. Res 106 (7), 14–733.
Henry, L.Y., Zimbelman, J.R., 1988. Physical Properties of Channels and Aeolian Features in the Oxia Palus and Margaritifer Sinus Quadrangles of Mars, pp. 479–480. LPSC XIX.
Kargel, J.S., 2004. Mars: A Warmer, Wetter Planet. Springer-Praxis, London. 557 pp.
Kargel, J.S., Marion, G.M., 2004. Mars as a Salt-, Acid-, and Gas-Hydrate World. LPSC XXXII. Abstract no. 1965.
Kieffer, H.H., Davis, P.A., Soderblom, L.A., 1981. Mars Global Properties—Maps and Applications, pp. 1395–1417. LPSC XIIB.
Krauskopf, K.B., 1979. Introduction to Geochemistry, 2nd ed. McGraw-Hill Book Co., New York. 617 pp.
Langevin, Y., Poulet, F., Bibring, J.P., Gondet, B., 2005. Sulfates in the North Polar Region of Mars Detected by OMEGA/Mars Express. InAmerican Association for the Advancement of Science, pp. 1584–1586.
Lee, S.W., 1984. Mars: wind streak production as related to obstacle type and size. Icarus 58 (3), 339–357.
Malin, M.C., Edgett, K.S., 2000. Sedimentary rocks of early Mars. Science 290 (5498), 1927–1937.
Marion, G.M., Catling, D.C., Kargel, J.S., 2003. Modeling aqueous ferrous iron chemistry at low temperatures with application to Mars. Geochimica et Cosmochimica Acta 67 (22), 4251–4266.
Marion, G.M., Kargel, J.S., Catling, D.C., 2007. Modeling ferrous–ferric iron chemistry with application to Martian surface geochemistry. Geochimica et Cosmochimica Acta (72), 242–266.
Maxwell, T.A., El-Baz, F., 1982. Analogs of Martian eolian features in the western desert of Egypt. In: El-Baz, F., Maxwell, T.A. (Eds.), Desert Landforms of Southwest Egypt: A Basis for Comparison with Mars, pp. 247–259. NASA Contract. Rep., CR-3611.
McCauley, J.F., Grolier, M.J., Breed, C.S., 1977. Yardangs. In: Doehring, D.O. (Ed.), Geomorphology in Arid Regions. Proceedings, 8th Annual Geomorphology Symposium, Binghamton, NY, pp. 233–272.
McCulloch, R.D., Bentley, M.J., Purves, R.S., Hulton, N.R.J., Sugden, D.E., Clapperton, C.M., 2000. Climatic inferences from glacial and paleoecological evidence at the Last Glacial termination, southern South America. Journal of Quaternary Science 15, 409–417.
Minitti, M.E., Mustard, J.F., Rutherford, M.J., 2002. Effects of glass content and oxidation on the spectra of SNC-like basalts—applications to Mars remote sensing. Journal of Geophysical Research. E. Planets 107, 6-1.
Moon, V., Jayawardane, J., 2004. Geomechanical and geochemical changes during early stages of weathering of Karamu Basalt, New Zealand. Engineering Geology 74 (1–2), 57–72.
Mustard, J.F., 1997. Are Dark Red Soils and Bright Dust on Mars Related through Mineralogic Phase Changes? pp. 1021–1022. LPSC XXVI.
O'Mahony, M., 1986. Sensory Evaluation of Food: Statistical Methods and Procedures. InCRC Press, p. 487.
Paruelo, J.M., Beltrőn, A., Jobbőgy, E., Sala, E.O., Golluscio, R.A., 1998. The climate of Patagonia: general patterns and controls on biotic processes. Ecologia Austral 8, 85–101.
Pelkey, S.H., J., B.M., M., M.T., 2001. Thermal inertia of crater related wind streaks on Mars. Journal of Geophysical Research 106, 23,909–23,920.
Peterfreund, A.R., 1981. Visual and infrared observations of wind streaks on Mars. Icarus 45 (2), 447–467.
Plinninger, R.J. and Thuro, K., 2004. Wear Prediction in Hard Rock Excavation Using the CERCHAR Abrasivity Index (CAI). EUROCK 2004 & 53rd Geocmechnics Colloquium (Scubert, Ed.), VGE, URL: http://www.geo.tum.de/people/thuro/pubs/2004_eurock_cai.pdf.
Poulet, F., Arvidson, R.E., Gomez, C., Morris, R.V., Bibring, J.P., Langevin, Y., Gondet, B., Griffes, J., 2008. Mineralogy of Terra Meridiani and western Arabia Terra from OMEGA/MEX and implications for their formation. Icarus 195, 106–130.
Presley, M.A., Arvidson, R.E., 1988. Nature and origin of materials exposed in the Oxia Palus–Western Arabia–Sinus Meridiani region, Mars. Icarus 75 (3), 499–517.
Rafkin, S.C.R., Michaels, T.I., 2003. Meteorological predictions for 2003 Mars Exploration Rover high-priority landing sites. Journal of Geophysical Research 108 (E12). doi:10.1029/2002JE002027.
Rickman, D. and Street, K.W., 2008. Some Expected Mechanical Characteristics of Lunar Dust from a Geological View. NASA Technical Report, Glenn Research Center, Marshall Space Flight Center, Document ID: 20080006059.
Rodriguez, J.A.P., Zimbelman, J., Kargel, J., Tanaka, K.L., Yamamoto, A., Sasaki, S., 2008. The Pali Aike Windstreak Field, Southern Patagonia, Argentina. LPSC, XXXIX(1518.pdf).
Sagan, C., Veverka, J., Fox, P., Dubisch, R., Lederberg, J., Levinthal, E., Quam, L., Tucker, R., Pollack, J.B., Smith, B.A., 1972. Variable features on Mars: preliminary Mariner 9 television results. Icarus 17 (2), 346–372.
Sagan, C., Toon, O.B., Gierasch, P.J., 1973. Climatic change on Mars. Science 181 (4104), 1045–1049.
Soderblom, L.A., Edwards, K., Eliason, E.M., Sanchez, E.M., Charette, M.P., 1978. Global color variations on the Martian surface. Icarus 34 (3), 446–464.
Spiga, A., Forget, F., Montabone, L., 2008. Study of the Martian boundary layer, mountain meteorology and 2001 dust storm with the LMD mesoscale model. Mars Atmosphere: Modeling and Observations 9028.pdf.
Squyres, S.W., Arvidson, R.E., Bell, J.F., Bruckner, J., Cabrol, N.A., Calvin, W., Carr, M.H., Christensen, P.R., Clark, B.C., Crumpler, L., 2004. The Opportunity Rover's Athena science investigation at Meridiani Planum, Mars. Science 306, 1698–1703.
Strickland, E.L., 1989. Physical Properties of Oxia/Lunae Planum and Arabia type units in the Central Equatorial Region of Mars, pp. 1079–1080. LPSC XX.
Swain, P.H., 1973. Pattern recognition: a basis for remote sensing data analysis. (LARS Information Note 111572). The Laboratory for Applications of Remote Sensing, Purdue University, West Lafayette, Indiana.
Szynkiewicz, A., Ewing, R.C., Moore, C.H., Giamoclija, M., Bustos, D., Pratt, L.M., 2010. Origin of Terrestrial Gypsum Dunes— Implications for Martian Gypsum-Rich Dunes of Olympia Undae. Geomorphology 121, 69–83 (this issue).
Thomas, P., 1984. Martian intracrater splotches: occurrence, morphology, and colors. Icarus 57 (2), 205–227.
Thomas, P., Veverka, J., 1979. Seasonal and secular variation of wind streaks on Mars—an analysis of Mariner 9 and Viking data. Journal of Geophysical Research 84 (8131–8146).
Thomas, P., Veverka, J., 1986. Red/violet contrast reversal on Mars: significance for eolian sediments. Icarus 66 (1), 39–55.
Thomas, P., Veverka, J., Lee, S., Bloom, A., 1981. Classification of wind streaks on Mars. Icarus 45, 124–153.
Thomas, P., Veverka, J., Gineris, D., Wong, L., 1984. “Dust” streaks on Mars. Icarus 60 (1), 161–179.
Tou, J.T., Rafael, C.G., 1974. Pattern Recognition Principles. Addison-Wesley Publishing Company, (Reading), Massachusetts.
Vaniman, D.T., Chipera, S.J., 2006. Transformations of Mg- and Ca-sulfate hydrates in Mars regolith. American Mineralogist 91 (10), 1628–1642.
Weischet, W., 1996. Regionale Klimatologie. Teil 1: Die neue Welt.-Teubner, Stuttgart, 468 pp.
Wyatt, M., McSween, H.Y., 2002. Spectral evidence for weathered basalt as an alternative to andesite in the northern lowlands of Mars. Nature 417, 263.
Wyatt, M.B., Bandfield, J.L., McSween Jr., H.Y., Christensen, P.R., 2001. Compositions of Low Albedo Intracrater Materials and Wind Streaks on Mars: Examination of MGS TES Data in Western Arabia Terra. LPSC XXXII. Abstract no. 1872.
Wyatt, M.B., McSween Jr., H.Y., Moersch, J.E., Christensen, P.R., 2003. Analysis of surface compositions in the Oxia Palus region on Mars from Mars Global Surveyor Thermal Emission Spectrometer observations. Journal of Geophysical Research 108 (E9), 11-1.

Zimbelman, J.R., 1986. Surface properties of the Pettit wind streak on Mars: implications for sediment transport. Icarus 66 (1), 83–93.
Zimbelman, J.R., Williams, S.H., 1996. Wind streaks: geological and botanical effects on surface albedo contrast. Geomorphology 17 (1–3), 167–185.
Zimbelman, J.R., Williams, S.H., 2002. Chemical indicators of separate sources for eolian sands in the eastern Mojave Desert, California, and western Arizona. Bulletin of the Geological Society of America 114 (4), 490–496.
Zimbelman, J.R., Williams, S.H., Tchakerian, V.P., 1995. Sand transport paths in the Mojave Desert, southwestern United States. In: Tchakerian, V.P. (Ed.), Desert Aeolian Processes. Chapman and Hall, New York, pp. 101–129.
Zolitschka, B., Schäbitz, F., Lücke, A., Wille, M., Mayr, C., Ohlendorf, C., Anselmetti, F., Ariztegui, D., Corbella, H., Ercolano, B., 2004. Climate changes in Southern Patagonia (Santa Cruz, Argentina) inferred from lake sediments—the multi-proxy approach of SALSA. PAGES News 12 (2), 9–11.
Zolitschka, B., Schabitzb, F., Luckec, A., Corbella, H., Ercolano, B., Fw, M., Haberzettl, T., Janssen, S., Maidana, N., Mayr, C., Ohlendorf, C., Oliva, G., Paez, M.M., Schleser, G.H., Soto, J., Tiberi, P., Wille, M., 2006. Crater lakes of the Pali Aike Volcanic Field as key sites for paleoclimatic and paleoecological reconstructions in southern Patagonia, Argentina. Journal of South American Earth Sciences 21 (294–309).